https://doi.org/10.5194/egusphere-2025-6099
Preprint. Discussion started: 23 December 2025
© Author(s) 2025. CC BY 4.0 License.

Aging of Droplet Size Distribution in Stratocumulus Clouds: Regimes of Droplet Size Distribution Evolution

Jung-Sub Lim[1, 2, 3] and Fabian Hoffmann[4]

[1]Meteorologisches Institut, Ludwig-Maximilians-Universität München, Munich, Germany
[2]Now at NOAA Chemical Science Laboratory, Boulder, CO, USA
[3]Now at Cooperative Institute for Research in Environmental Sciences, University of Colorado, Boulder, CO, USA
[4]Freie Universität Berlin, Berlin, Germany

Correspondence: Fabian Hoffmann (f.hoffmann@fu-berlin.de)

Abstract. The climatic impact of maritime stratocumulus clouds depends on the evolution of their droplet size distribution (DSD), yet the mechanisms controlling its variability during evaporation remain poorly constrained. Using large-eddy simulations coupled with a Lagrangian cloud model, we demonstrate that the evolution of the DSD exhibits two primary regimes: an adiabatic growth regime and an entrainment–descent regime. Within the latter, DSD evolution follows divergent pathways determined by the droplet's history: direct mixing of entrained air near the cloud top causes rapid broadening, whereas large-scale boundary-layer descent leads to gradual evaporation. Our Lagrangian analysis of the Damköhler number reveals that the commonly observed vertical transition from inhomogeneous to homogeneous mixing signatures does not necessarily reflect a change in the mixing mechanism. Instead, it results from the divergent histories of droplets that are either mixed with dry air or remain undiluted. Droplets directly impacted by entrainment retain inhomogeneous signatures throughout their descent, while those unaffected by direct mixing exhibit homogeneous-like characteristics regardless of altitude. This distinction helps resolve ambiguities in interpreting in situ observations where mixing history is often unknown. Finally, we propose a combined analytical–empirical formulation that captures the relative dispersion during both growth and evaporation.

1 Introduction

Maritime stratocumulus (Sc) clouds play a key role in Earth's climate by cooling the planet through the reflection of large amounts of incoming solar radiation (Chen et al., 2000; Siebesma et al., 2004; Wood, 2012). Stratocumulus-topped boundary layers (STBLs) are characterized by a Rayleigh-Bénard-type circulation, driven predominantly by longwave radiative cooling at the cloud top (e.g., Wood, 2012; Mellado, 2017). This circulation is characterized by broad, cloud-laden updrafts and narrow, nearly cloud-free downdrafts known as *cloud holes* (e.g., Krueger, 1993; Korolev and Mazin, 1993; Gerber et al., 2005). As droplets cycle through this dynamic environment, they undergo activation, condensational growth, entrainment-driven evaporation, and circulation-induced descent, leading to systematic changes in the droplet size distribution (DSD). The DSD is a fundamental parameter affecting cloud optical properties (Considine and Curry, 1996; Pawlowska et al., 2006; Chandrakar et al., 2022) and precipitation initiation (Seifert and Beheng, 2006).

https://doi.org/10.5194/egusphere-2025-6099
Preprint. Discussion started: 23 December 2025
© Author(s) 2025. CC BY 4.0 License.

To capture the time-dependent transformation of cloud microphysics, we define "DSD aging" as the temporal evolution of its shape. Although this concept has previously been introduced in the context of precipitation initiation (Seifert and Beheng, 2006), we specifically use it here to describe the microphysical evolution of the DSD driven by condensation, evaporation, entrainment, and mixing. We characterize DSD aging using two key parameters: the mean droplet radius (r_{m}) and the relative dispersion (d_{r}), defined as the ratio of the standard deviation to the mean radius. The relative dispersion d_{r} describes the relative width of the size distribution. It is a key determinant of both cloud optical properties and rain initiation (Liu and Daum, 2004; Liu et al., 2008; Wang et al., 2021), yet it is rarely predicted in conventional moment-based microphysical models. Therefore, understanding DSD aging within the STBL is essential for improving cloud–aerosol–precipitation interactions in climate models, as it links intricate DSD shapes to more predictable boundary layer dynamics.

Previous studies have shown that the correlation between d_{r} and r_{m} varies depending on the dominant microphysical processes and environmental conditions. In particular, this correlation can shift between positive and negative across different stages of droplet evolution (Chandrakar et al., 2018; Lu et al., 2020; Luo et al., 2022). For instance, in an adiabatically ascending parcel, condensational growth increases r_{m} and decreases d_{r}, as smaller droplets grow faster, leading to a narrower DSD (Yau and Rogers, 1996). This inverse relationship during adiabatic ascent can be described by a simple analytical expression (Liu et al., 2006).

However, during entrainment and mixing, the changes in r_{m} and d_{r} become more complex and less predictable. This complexity arises because entrainment is a non-adiabatic and transient process. The amount of free-tropospheric air that is entrained, the rate at which it mixes with cloudy air, and the timescale over which the mixture approaches thermodynamic equilibrium, all of which are critical for understanding how entrainment and mixing influence DSD shape, remain poorly constrained in both observations and models. In addition, the specific mixing scenario further complicates predictions. Under homogeneous mixing, r_{m} typically decreases and d_{r} increases as all droplets partially evaporate (Baker and Latham, 1979). In contrast, inhomogeneous mixing may leave both parameters largely unchanged while decreasing the droplet number concentration through the complete evaporation of some droplets (Baker and Latham, 1979; Baker et al., 1980; Lehmann et al., 2009). Even r_{m} can increase and d_{r} decrease in a "narrowing" mixing scenario as suggested in a recent study (Lim and Hoffmann, 2023). In situ measurements often reveal inhomogeneous mixing signatures near the cloud top and homogeneous characteristics below (Yum et al., 2015; Yeom et al., 2021). However, it remains unclear whether this reflects a true change in the physical mixing mechanism or results from other processes, such as dilution or the vertical sorting of droplets with different mixing histories. Therefore, to understand the spatiotemporal variability of d_{r} in stratocumulus clouds, it is essential to resolve how entrainment and mixing interact with the Lagrangian history of the droplets.

In this study, we employ the L^3 model (Hoffmann et al., 2019; Hoffmann and Feingold, 2019; Lim and Hoffmann, 2023, 2024), a novel framework that combines large-eddy simulation (LES) with a linear eddy model (LEM) and a Lagrangian cloud model (LCM). The L^3 model explicitly resolves subgrid-scale (SGS) supersaturation (S) fluctuations and turbulent mixing using the LEM, which mimics fine-scale turbulent stirring and scalar transport (Kerstein, 1988). The LCM tracks individual hydrometeors (e.g., Hoffmann et al., 2015), represented as computational particles that stand in for ensembles of real droplets or aerosols (Shima et al., 2009), thereby capturing detailed microphysical processes. This Lagrangian approach enables us to track in-

https://doi.org/10.5194/egusphere-2025-6099
Preprint. Discussion started: 23 December 2025
© Author(s) 2025. CC BY 4.0 License.

dividual particles along their trajectories through the STBL vertical circulation, capturing the evolving thermodynamic and microphysical conditions that govern droplet growth. In particular, it allows for a detailed quantification of how the DSD shape evolves along distinct pathways shaped by droplet activation, condensation, entrainment, mixing, and evaporation.

This paper is structured as follows. Section 2 presents the L^3 model framework and simulation settings. Section 3 shows how the DSD shape parameters evolve in different regimes. Finally, we conclude our paper in Sec. 4. In Appendix A we discusses a method to predict d_r in these regimes. Parts of this study are based on the first author's dissertation (Lim, 2024), which has been extended with special attention to the impact of different mixing pathways (Sec. 3.3.3 and 3.4) and more general conclusions (Sec. 4).

2 Model and Simulations

2.1 The L^3 model

We employ the novel L^3 model (Hoffmann et al., 2019), built upon the System for Atmospheric Modeling (SAM), a non-hydrostatic, anelastic LES model (Khairoutdinov and Randall, 2003). Cloud microphysical processes are modeled using the LCM, employing individually simulated computational particles, i.e., LCM particles, where each particle represents a group of identical hydrometeors. Additionally, the linear eddy model (LEM), an explicit turbulence and mixing model (Kerstein, 1988; Krueger et al., 1997), is coupled with the LCM and LES to represent the unresolved effects of entrainment and mixing on droplet growth (Hoffmann et al., 2019; Hoffmann and Feingold, 2019; Lim and Hoffmann, 2023, 2024).

In the Lagrangian Cloud Model (LCM), condensational growth of droplets is driven by the supersaturation,

$$S = \bar{S} + S', \tag{1}$$

where the LES-resolved mean supersaturation is

$$\bar{S} = \frac{\bar{q}_\mathrm{v}}{q_\mathrm{s}(\bar{T}, p)} - 1. \tag{2}$$

Here, $\bar{q}_\mathrm{v}$ is the LES-resolved water vapor mixing ratio, and q_s is the saturation vapor mixing ratio determined by the LES-resolved temperature $\bar{T}$ and pressure p. The fluctuation term S' represents the deviation from $\bar{S}$ and is tracked individually for each LCM particle, being updated continuously throughout its growth history. The LEM redistributes S' among the LCM particles by mimicking turbulent compression and folding based on the LES subgrid turbulence kinetic energy. Therefore, in the L^3 model, droplet condensational growth is determined by both $\bar{S}$ and S', allowing for a realistic representation of different mixing scenarios during entrainment and mixing (Lim and Hoffmann, 2023, 2024). Moreover, the standard deviation of supersaturation, σ_S, defined as the standard deviation of $S = \bar{S} + S'$, is inherently resolved by the L^3 model. Further details on the L^3 framework can be found in Hoffmann et al. (2019).

https://doi.org/10.5194/egusphere-2025-6099
Preprint. Discussion started: 23 December 2025
© Author(s) 2025. CC BY 4.0 License.

2.2 Simulation Setup

A maritime nocturnal Sc cloud is simulated based on the second dynamics and chemistry of Marine Stratocumulus Field Study (DYCOMS-II) campaign (Stevens et al., 2003), with fixed surface fluxes, subsidence, and a simple parameterization for longwave radiative cooling (Ackerman et al., 2009). The model domain is 3.2 km × 3.2 km × 2.56 km in x, y, and z directions, with a 10 m × 10 m × 5 m grid spacing, respectively. This high-resolution setup is essential for resolving the small-scale turbulent structures, which are critical to representing entrainment and mixing. The model time step $\delta t = 0.5$ s, and the total model integration time is 5 h. The results are analyzed only for the last 2 h of the simulation.

The LCM particles, each representing the same number of hydrometeors, are initialized as sea-salt particles with dry radii randomly chosen from a log-normal distribution (geometric mean radius of $r_{\mathrm{m,a}} = 80$ nm, geometric standard deviation $\sigma_{\mathrm{r}} = 1.4$). Initial aerosol number concentrations of $N_{\mathrm{a}} = 50$, 100, and 200 cm^{-3} are considered, named N50, N100, and N200, respectively. Results are discussed mainly for the N100 case unless otherwise stated. Note that droplet sedimentation and collision-coalescence processes are not considered, since we focus on the evolution of the DSD shape in non-drizzling Sc.

The LEM further complements the high resolution of the LES. In the L^3 model, the vertical LES grid spacing (Δz_{LES}) and the number of LCM particles per grid box (n_{p}) jointly determine the resolution of the LEM, defined as $\Delta z_{\mathrm{LEM}} = \Delta z_{\mathrm{LES}}/n_{\mathrm{p}}$. In this simulation, we initialize 100 LCM particles per grid box, resulting in a Δz_{LEM} of approximately 5 cm, which is sufficient to resolve all relevant scales of inhomogeneous mixing in Sc clouds (Hoffmann and Feingold, 2019).

For post-analysis, a subset of 200 LCM particles within the cloud region is selected and tracked throughout the simulation, where the cloud region is defined by a cloud water mixing ratio $q_{\mathrm{c}} \geq 0.01\ \mathrm{g\,kg}^{-1}$. At each time step, the properties of the LES grid box (e.g., pressure, temperature, vapor pressure) and those of the LCM particles (e.g., droplet radius and position) within the same grid box are recorded. Note that properties along the LCM particle trajectories are smoothed using a Gaussian kernel filter (Virtanen et al., 2020), with a window size of 10 s to reduce noise.

3 Results

3.1 Dynamical and Mixing Characteristics of the STBL

We begin by characterizing the dynamical and mixing structure of the STBL. Figure 1a shows the mean vertical profile of two moist-adiabatically conserved variables: total water mixing ratio (q_{t}) and liquid water potential temperature (θ_{l}). The STBL consists of a well-mixed layer, characterized by high q_{t} and low θ_{l}, the free troposphere with low q_{t} and high θ_{l}, and an entrainment interface layer (EIL) in between. The EIL is characterized by sharp gradients in both moisture and temperature, typically within a few tens of meters. It represents the transition zone where turbulent eddies from the boundary layer mix with overlying dry and warm free-tropospheric air. Based on the sharp contrast in q_{t} and θ_{l} between the boundary layer and the free troposphere, we define a mixing fraction,

$$\chi = \frac{(q_{\mathrm{t}} - q_{\mathrm{t,bl}})}{(q_{\mathrm{t,ft}} - q_{\mathrm{t,bl}})}, \tag{3}$$

https://doi.org/10.5194/egusphere-2025-6099
Preprint. Discussion started: 23 December 2025
© Author(s) 2025. CC BY 4.0 License.

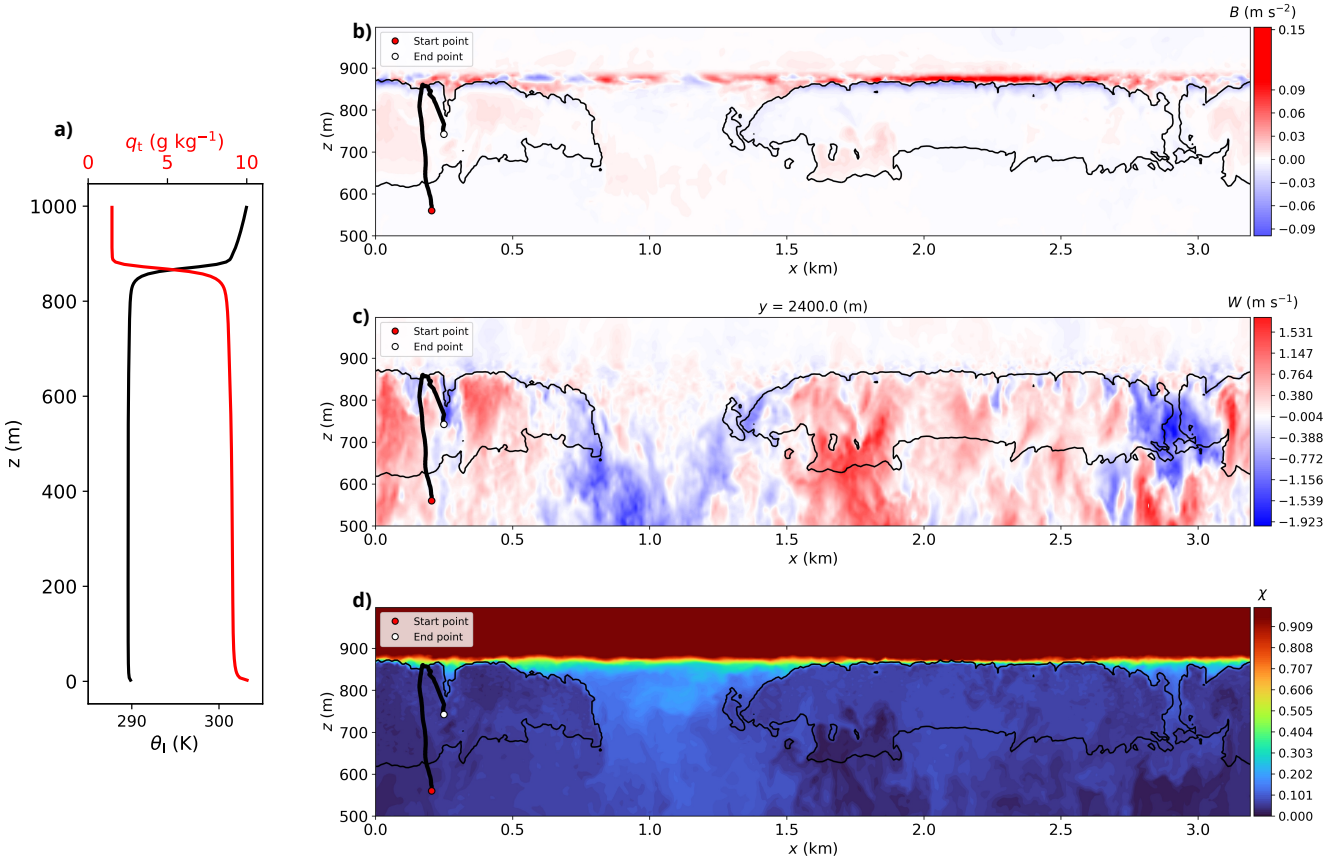

Figure 1. a) Vertical profiles of q_t (red solid line) and θ_l (black solid line). Vertical cross-sections of b) buoyancy B, c) vertical velocity W, and d) mixing fraction χ at $y = 2400$ m and at 13320 s simulation time. In panels b), c), and d), the trajectory of a particle is shown as a thick black line, starting from the red dot at $t = 12298.5$ s and ending at the white dot at $t = 13320$ s. The black solid lines indicate where the cloud water mixing ratio $q_c = 0.01$ g kg^{-1}.

which represents the fraction of free-tropospheric air mixed with boundary-layer air. In this simulation, χ is estimated using q_t, where $q_{t,ft}$ and $q_{t,bl}$ are set to their initial values of 1.5 and 9.5 g kg^{-1}, respectively, which remain nearly constant throughout the simulation.

120 At the top of the STBL, stable stratification inhibits mixing between the boundary layer and the free troposphere. Consequently, χ is also strongly stratified (Fig. 1d), with the most rapid change confined to the EIL, identifying this region as the primary site of entrainment and mixing. The cloud top and EIL are persistently negatively buoyant (Fig. 1b), where the buoyancy is defined by

$$B = g\left(\frac{\theta_v - \bar{\theta}_v}{\bar{\theta}_v}\right) \tag{4}$$

https://doi.org/10.5194/egusphere-2025-6099
Preprint. Discussion started: 23 December 2025
© Author(s) 2025. CC BY 4.0 License.

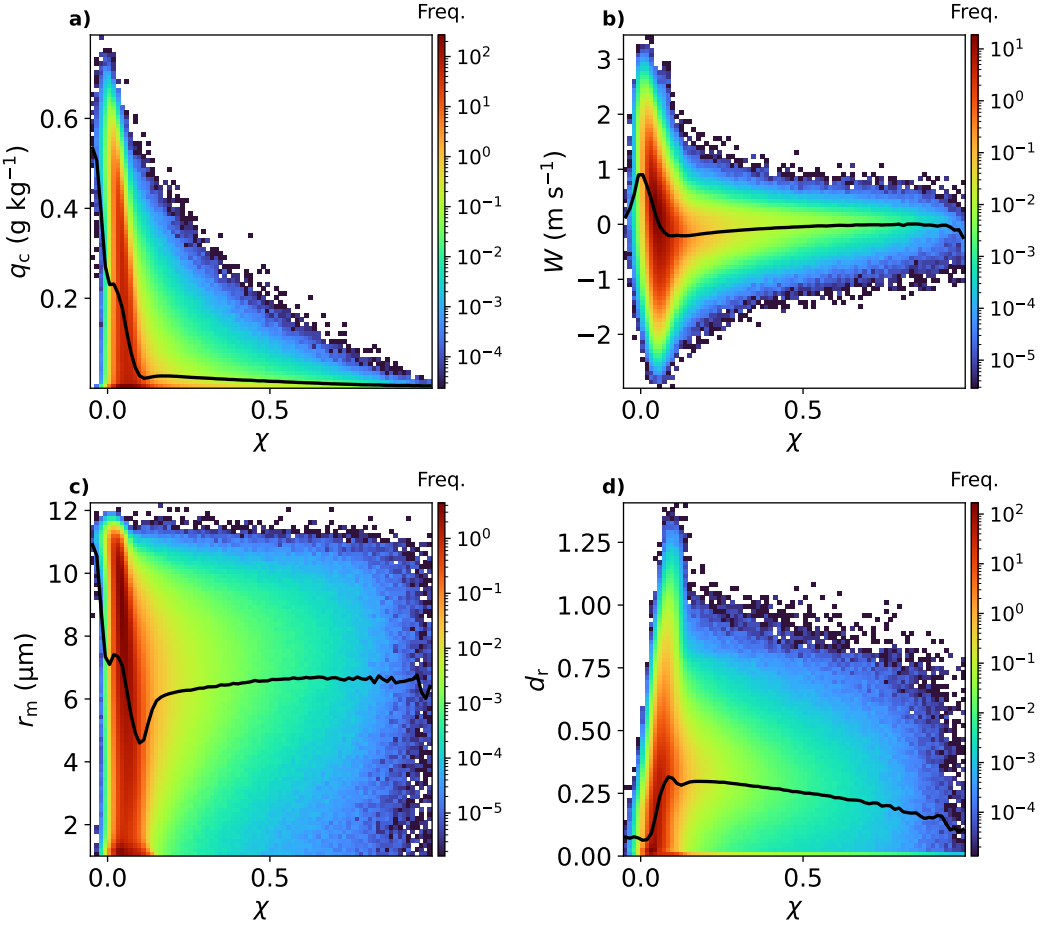

Figure 2. Two-dimensional density histograms of χ versus a) q_c, b) W, c) r_m, and d) d_r, with black solid lines indicating the mean of each variable in bins of χ.

where g is the gravitational acceleration, and θ_v and $\bar{\theta}_v$ are the local and horizontally averaged virtual potential temperatures, respectively. The negative B arises from evaporative cooling during entrainment and longwave radiative cooling (Stevens, 2002; Wood, 2012).

High values of χ are rarely observed within the cloud interior. However, localized pockets of enhanced χ can appear within the boundary layer, particularly near cloud holes and in descending branches of the STBL vertical circulation ($W < 0$ m s^{-1}, Fig. 1c). For example, at $x = 0.2$ km and $x = 3$ km, cloud holes coincide with downdrafts and elevated χ, possibly indicating the accumulation of previously entrained dry air.

While χ can highlight regions influenced by entrainment, its relationship with microphysical variables such as r_m and d_r is not straightforward. To explore this quantitatively, Fig. 2 illustrates the relationships between various variables and χ. q_c is negatively correlated with χ, with high q_c (> 0.5 g kg^{-1}) occurring only in regions with very low χ (< 0.1), corresponding to

https://doi.org/10.5194/egusphere-2025-6099
Preprint. Discussion started: 23 December 2025
© Author(s) 2025. CC BY 4.0 License.

undiluted, nearly adiabatic cloud interiors. Notably, all panels show a dense cluster around $\chi < 0.1$, suggesting a prevalence of nearly adiabatic cloud interior during both ascent and descent (Fig. 2b). High values of χ are associated with $-1\ \mathrm{m\,s^{-1}} < W < 1\ \mathrm{m\,s^{-1}}$, a range typically found in regions experiencing entrainment and mixing at the cloud top under near-neutral conditions.

Figures 2c and d show that r_m tends to decrease and d_r tends to increase with increasing χ in regions that remain nearly adiabatic ($\chi < 0.1$). However, when $\chi > 0.1$, the mean values flatten out, and the relationship becomes less clear: neither r_m nor d_r shows a strong or consistent dependence on χ. This suggests that while χ may correlate with microphysical variability in undiluted cloud regions, it alone cannot explain the droplet size evolution in environments influenced by entrainment and mixing. Therefore, to gain a more comprehensive understanding of the evolution of r_m and d_r, especially under the influence of entrainment and mixing, it is essential to consider the full growth history of individual droplets.

To illustrate this approach, Figures 1 and 3 show an example particle trajectory that captures a representative pathway within the STBL vertical circulation. Droplets along this path undergo four key microphysical stages: i) activation near the cloud base, ii) condensational growth in updrafts, iii) entrainment and mixing at the cloud top, and iv) descent, evaporation, and deactivation. These stages leave clear imprints on the evolution of r_m and d_r. While both r_m and q_c generally increase with height in cloudy updrafts, a sharp decrease occurs near cloud holes (Fig. 3a, b), reflecting the effects of mixing and evaporation. In contrast, d_r shows a more complex distribution: it is typically lower inside clouds but increases near cloud top and cloud-hole boundaries (Fig. 3c), resembling the spatial structure of χ (Figs. 1d and 3d). In the following sections, we examine how particle histories shape distinct DSD aging regimes and control the evolution of r_m and d_r.

3.2 Droplet Evolution Pathways in the r_m–d_r Phase Space

To further understand the evolution of r_m and d_r, we analyze the droplet evolution in the r_m–d_r phase space. Figure 4a shows the frequency distribution of the r_m–d_r phase space obtained from three-dimensional model output, where, r_m and d_r are estimated from cloud droplets with radii > 1 μm only. Overall, the range of d_r is inversely proportional to r_m, with $d_\mathrm{r} = 1.0$ at $r_\mathrm{m} = 3$ μm and $d_\mathrm{r} \to 0$ for $r_\mathrm{m} = 12$ μm. The high-frequency pattern visible in Fig. 4a is divided into two distinct parts, which can be constrained by S (Fig. 5). We define these as the 'growth pathway' characterized by low d_r for $S \geq 0$ and hence condensational growth (Fig. 5c and d), and the 'evaporation pathway' characterized by high d_r for $S < 0$ and hence evaporation (Fig. 5e and f). Thus, we expect a quasi-loop structure of droplet evolution from the growth pathway to the evaporation pathway. Figure 4b shows the LCM particle trajectories in this phase space, with black and green markers indicating the start and end points, respectively, and the corresponding frequency distribution in Fig. 4c. Note that the high-density patterns resemble the two pathways identified in the model output frequency distribution (Fig. 4a). In this analysis, we treat each continuous in-cloud segment of a particle trajectory as an independent trajectory, as a single particle can enter the cloud multiple times. This results in a total of 384 trajectory segments. We confirm that the qualitative features of Fig. 4 and other analyses presented later in this study (e.g., Fig. 5) remain unchanged when using subsets of 100 or 200 trajectories, indicating that the results are robust with respect to sample size throughout the analysis.

https://doi.org/10.5194/egusphere-2025-6099
Preprint. Discussion started: 23 December 2025
© Author(s) 2025. CC BY 4.0 License.

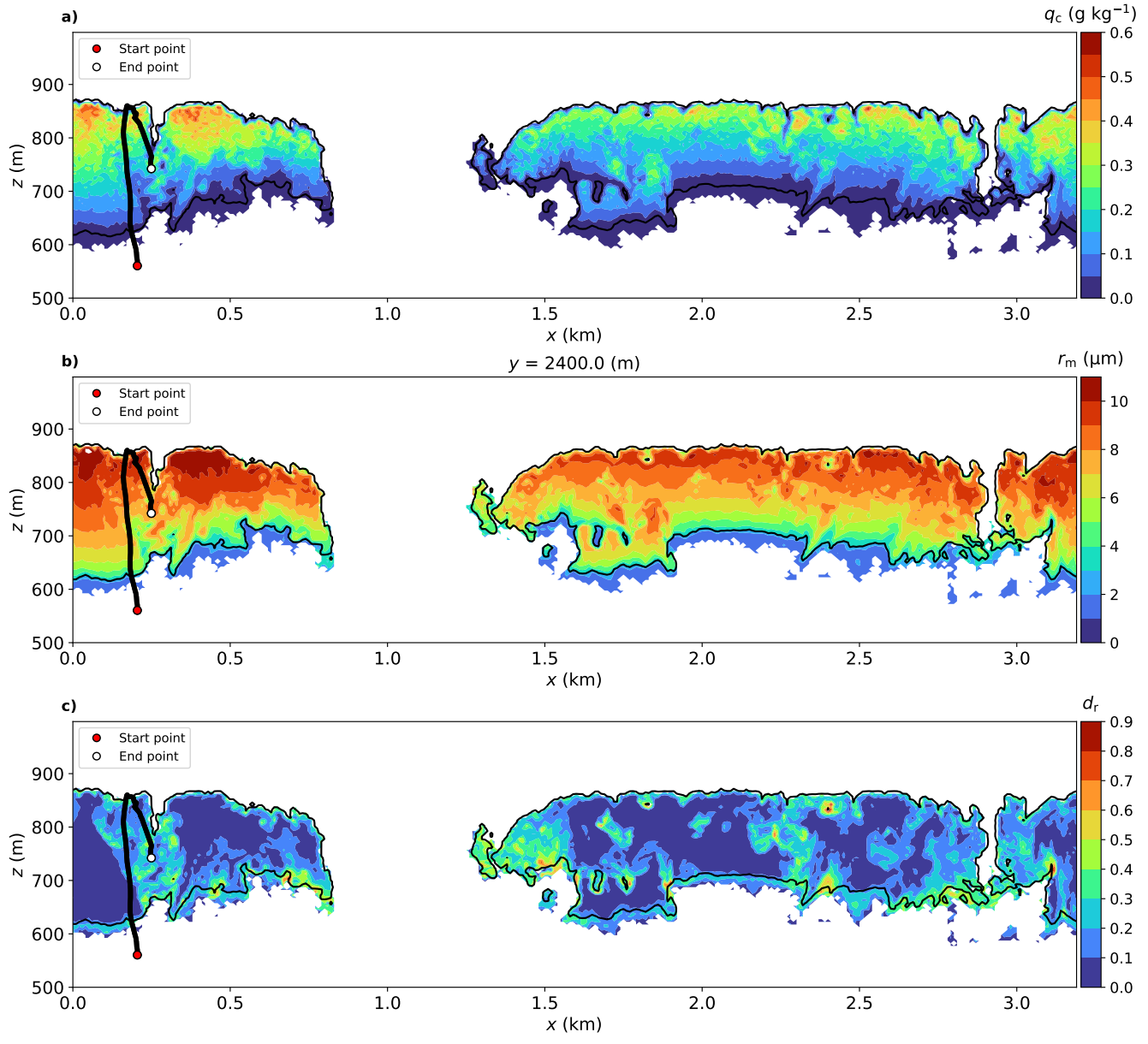

Figure 3. Vertical cross-sections of a) q_c, b) r_m, and c) d_r at $y = 2400$ m and at 13320 s of simulation time. The trajectory of the particle located at the end point (white dot) at this time is shown as a thick black line, starting from the red dot. The thin black lines in each panel indicate where the cloud water mixing ratio $q_c = 0.01$ g kg^{-1}.

The growth pathway can be described by

$$d_r = d_{r,0} \frac{r_{m,0}^2}{r_m^2}, \tag{5}$$

https://doi.org/10.5194/egusphere-2025-6099
Preprint. Discussion started: 23 December 2025
© Author(s) 2025. CC BY 4.0 License.

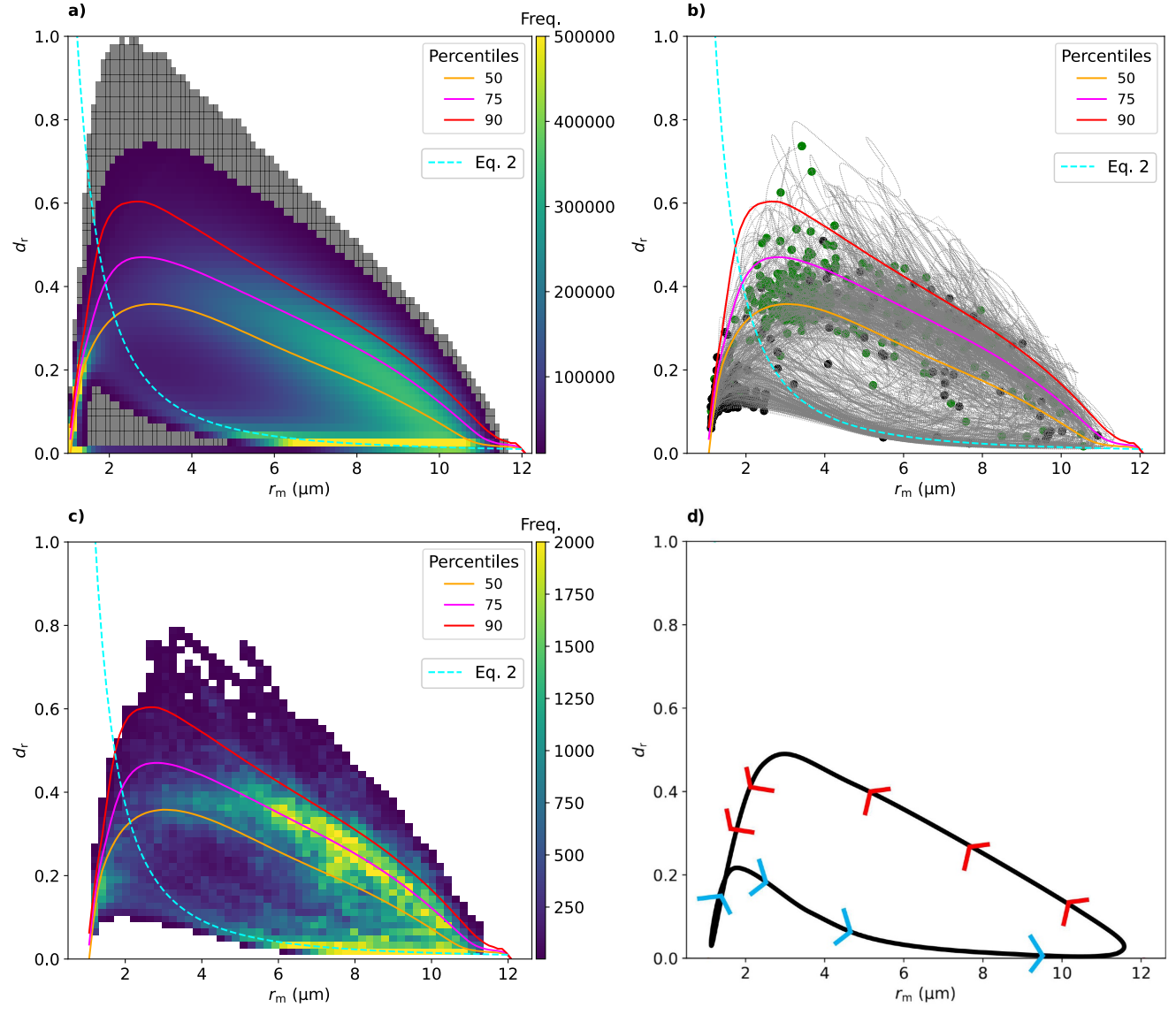

Figure 4. a) Contour plot of the frequency distributions in r_m and d_r phase space. b) Corresponding droplet evolution pathways (gray dotted lines) with start/end points in black/green. c) The corresponding frequency distribution of droplet evolution pathways. d) Conceptual schematic summarizing the composite evolution loop, constructed from the most frequently observed trajectory patterns in the r_m–d_r phase space. Blue and red arrows represent the dominant directions of growing and decaying pathways, respectively, based on the Lagrangian trajectory. In each panel, 50th, 75th, and 90th percentiles at each r_m value and Eq. 5 are indicated as solid lines in orange, magenta, red, and cyan, respectively.

following the analytic solution proposed by Liu et al. (2006), where $d_{r,0}$ and $r_{m,0}$ denote the boundary values. Here, we use $d_{r,0} = 0.01$ and $r_{m,0} = 12$ μm to show Eq. 5 as a cyan dashed line in Fig. 4a and b.

https://doi.org/10.5194/egusphere-2025-6099
Preprint. Discussion started: 23 December 2025
© Author(s) 2025. CC BY 4.0 License.

While Eq. 5 effectively captures the growth pathway, it fails to describe the evaporation pathway (Fig. A1). To approximate the latter, we utilize percentile-based diagnostics, where the 50th, 75th, and 90th percentiles of d_r at each r_m bin provide a reasonable empirical representation of the evaporation pathway (Fig. 4a–c), exhibiting an inverse trend between d_r and r_m. In analogy to Eq. 5, the fitted function is given as

$$d_\mathrm{r} = d_\mathrm{r,max}\left(1 - \frac{r_\mathrm{m}^2}{r_\mathrm{m,max}^2}\right), \tag{6}$$

where $r_\mathrm{m,max}$ and $d_\mathrm{r,max}$ denote the maximum values of r_m and d_r, respectively. Each percentile line (p50, p75, and p90) can be represented by a distinct $d_\mathrm{r,max}$ value for the same r_m (e.g., Fig. 4a). For instance, d_r approaches zero as r_m approaches $r_\mathrm{m,max}$, whereas $d_\mathrm{r,max}$ typically occurs at much smaller droplet sizes (e.g., $r_\mathrm{m} < 3$ µm), well below $r_\mathrm{m,max}$. A detailed derivation is provided in Appendix A.

3.3 Different Regimes of Droplet Evolution Pathways

In the previous section, we showed that droplet evolution pathways diverge depending on whether droplets grow or decay. To better characterize these differences, we analyze the r_m–d_r phase space in terms of the sign of the correlation between $\dot{d}_\mathrm{r} \equiv \mathrm{d}d_\mathrm{r}/\mathrm{d}t$ and $\dot{r}_\mathrm{m} \equiv \mathrm{d}r_\mathrm{m}/\mathrm{d}t$. This analysis uses the particle trajectories shown in Fig. 4b and c.

As already indicated above, the resulting patterns are closely tied to the supersaturation S. As shown in Fig. 5a and b, the phase space structure under all S conditions can be decomposed into two dominant subsets based on $S \geq 0$ and $S < 0$ (second and third rows). While the droplet life cycle is a continuous process, we can classify it into four distinct regimes, each characterized by a dominant set of microphysical processes: A (*activation*) and B (*adiabatic growth*) for $S \geq 0$, and C (*entrainment and descent*) and D (*deactivation*) for $S < 0$, each of which corresponds to a dominant microphysical processes. Although precipitation is another key process in DSD evolution, we focus on condensational growth and evaporation, examining phase-space–averaged microphysical and environmental properties across the four regimes (Figs. 6 and 7).

3.3.1 Activation Regime ($S \geq 0$)

In the *activation regime*, the $\dot{r_\mathrm{m}}$–$\dot{d}_\mathrm{r}$ correlation is primarily positive (region A in Fig. 5c and d), especially when $r_\mathrm{m} < 2$ µm. This regime is associated with droplet activation occurring in updrafts (Fig. 7b) near the cloud base (Fig. 7c), as indicated by high net activation rates (Fig. 6g). The corresponding increase in droplet number concentration (Fig. 6c) marks cloud formation. In Fig. 4b, most particle trajectories initiate within this regime (black dots). During this phase, condensational growth increases r_m, while the time-dependent activation of aerosols with different critical supersaturations leads to an increase in d_r. This results in a transient broadening of the DSD, prior to narrowing due to subsequent condensational growth.

3.3.2 Adiabatic Growth Regime ($S \geq 0$)

Following the *activation regime*, droplets enter the *adiabatic growth regime* (region B in Fig. 5c and d), particularly when $d_\mathrm{r} < 0.1$. In this regime, cloud droplets grow by condensation within regions of high supersaturation (Fig. 6g), strong updrafts

https://doi.org/10.5194/egusphere-2025-6099
Preprint. Discussion started: 23 December 2025
© Author(s) 2025. CC BY 4.0 License.

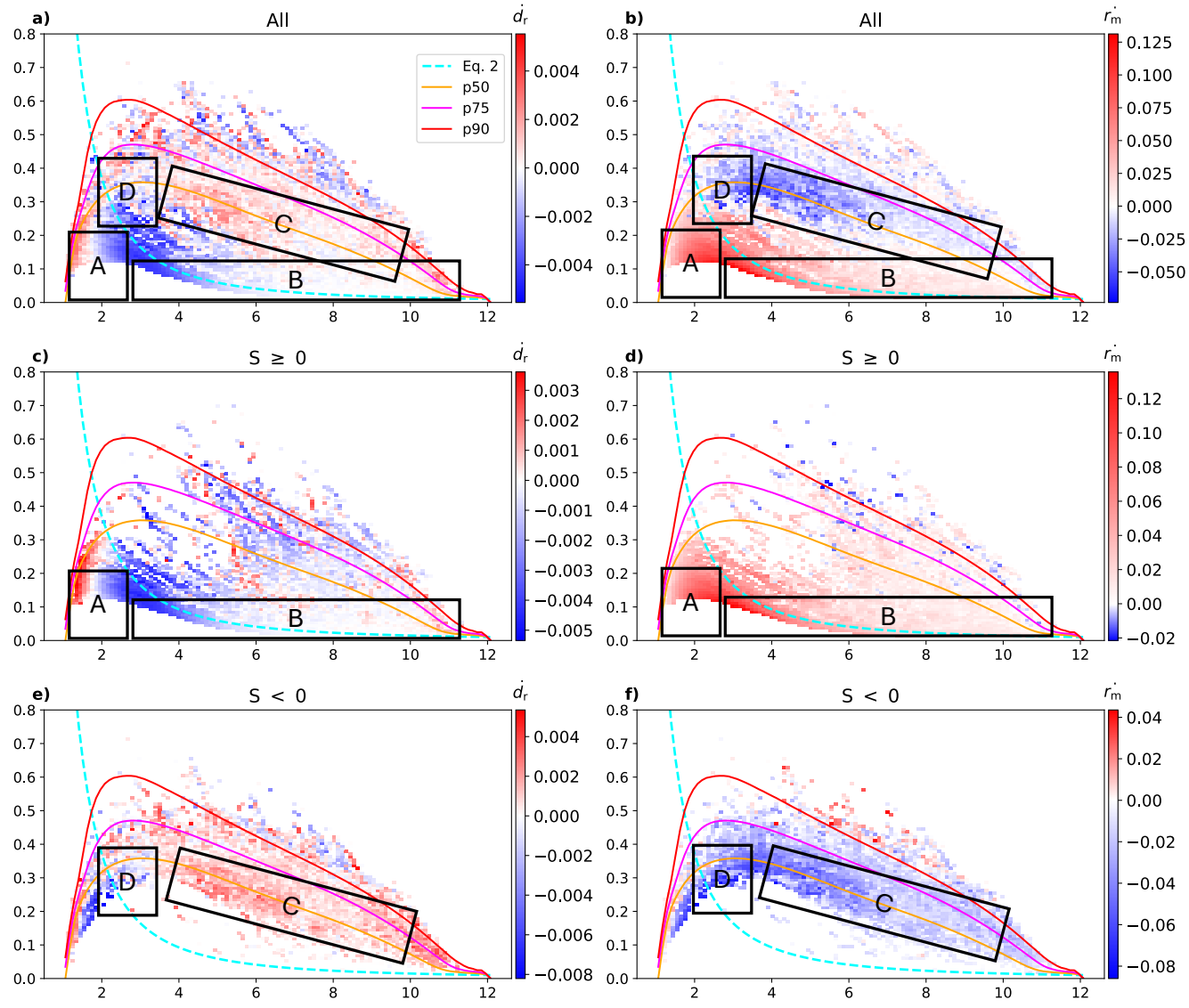

Figure 5. Contour plots of $\dot{d}_r$ (first column) and $\dot{r}_m$ (second column) in the r_m-d_r phase space for all conditions (first row), $S \geq 0$ (second row), and $S < 0$ (third row). In each panel, the 50th, 75th, and 90th percentile values (p50, p75, p90), and Eq. 5 from Fig. 4 are indicated by solid lines in orange, magenta, red, and cyan, respectively. Each panel shows 2D binned mean values of $\dot{d}r$ and $\dot{r}m$ in the r_m–d_r phase space, based on Lagrangian trajectories smoothed with a Gaussian kernel (window = 10 s) and averaged over time.

(Fig. 7b), and low mixing fraction χ (Fig. 6h). Activation and deactivation are negligible (Fig. 6i), resulting in an almost constant droplet number concentration, N_c (Fig. 6c). The turbulent kinetic energy dissipation rate (ε) remains low (Fig. 7g), indicating weak turbulence. In addition, the small standard deviation of supersaturation, σ_S (Fig. 7h), indicates a highly homo-
205 geneous supersaturation field, implying minimal entrainment and mixing-driven dilution of the cloudy air.

https://doi.org/10.5194/egusphere-2025-6099
Preprint. Discussion started: 23 December 2025
© Author(s) 2025. CC BY 4.0 License.

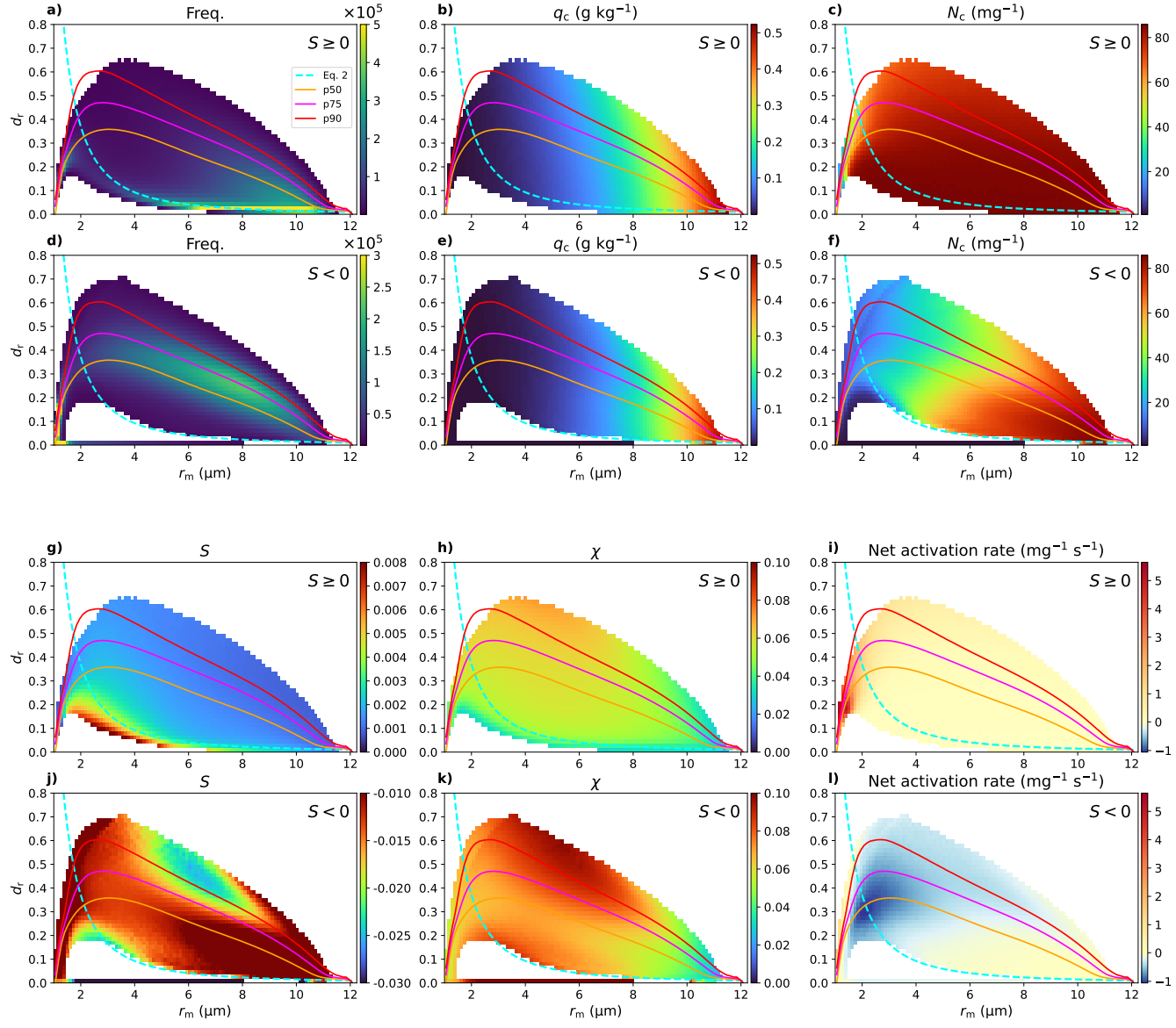

Figure 6. Contour plots of cloud properties in the r_{m} and d_{r} phase space for $S \geq 0$ (first and third row) and $S < 0$ (second and fourth row). a) and d) show the frequency distributions, b) and e) show cloud water mixing ratio (q_{c}), c) and f) show cloud droplet number concentration (N_{c}), g) and j) show the mean supersaturation (S), h) and k) show mixing fraction (χ) and i) and l) show net activation rate (activation rate - deactivation rate). In each panel, the 50th, 75th, and 90th percentile values (p50, p75, p90), and Eq. 5 from Fig. 4 are indicated by solid lines in orange, magenta, red, and cyan, respectively. Values represent bin-averaged means from 3D simulation results during the final 2 hours of simulation, mapped onto the r_{m}–d_{r} phase space.

In this regime, $\dot{r}_{\mathrm{m}}$ and $\dot{d}_{\mathrm{r}}$ exhibit a negative correlation, reflecting classical condensational growth behavior: the radius of small droplets grows faster, narrowing the DSD as its mean size increases. This behavior aligns with parcel theory and is typically observed within the adiabatic cores of stratocumulus clouds (Yau and Rogers, 1996; Liu et al., 2006).

https://doi.org/10.5194/egusphere-2025-6099
Preprint. Discussion started: 23 December 2025
© Author(s) 2025. CC BY 4.0 License.

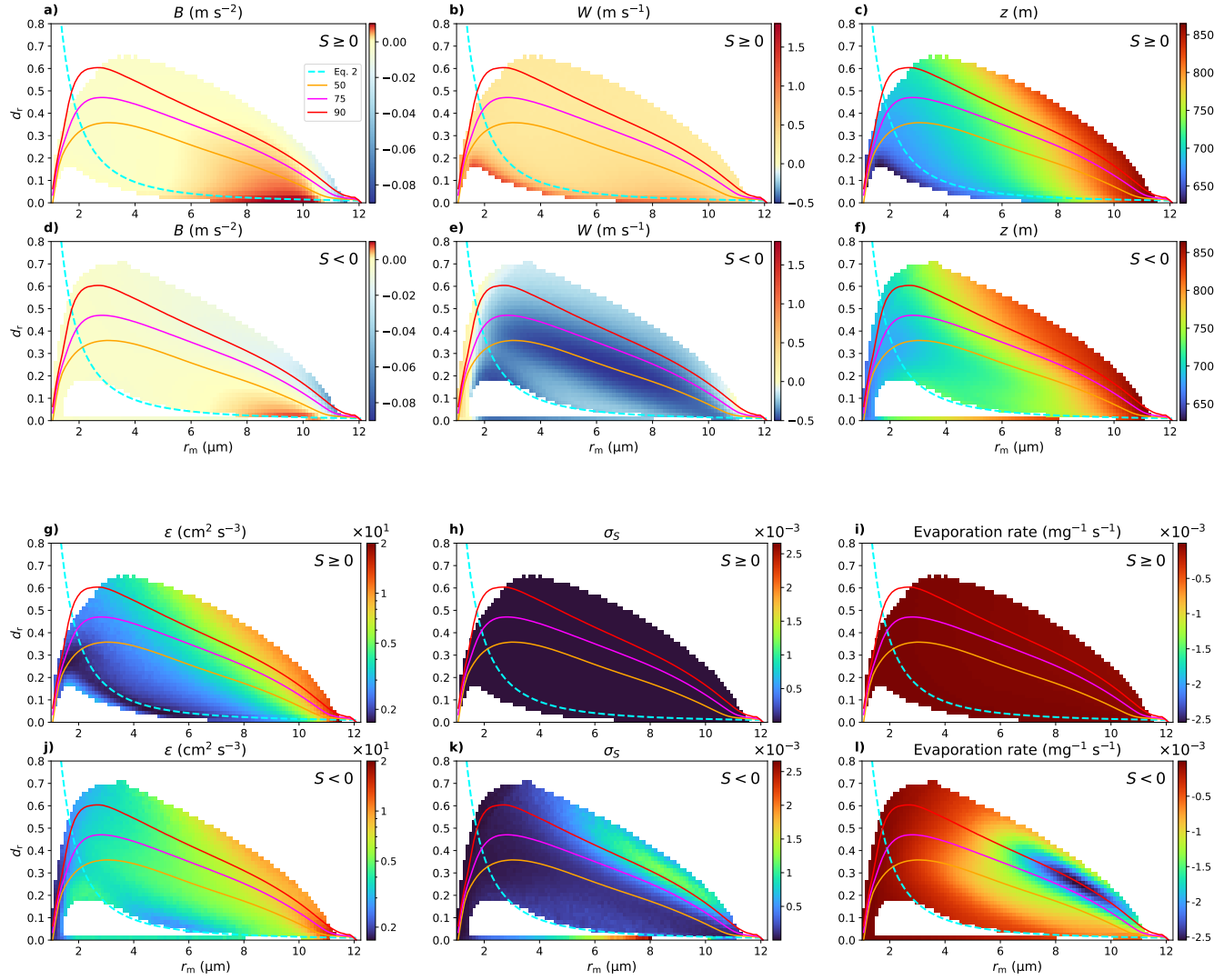

Figure 7. Contour plots of cloud properties in the r_{m} and d_{r} phase space for $S \geq 0$ (first and third row) and $S < 0$ (second and fourth row). a) and d) show buoyancy (B), b) and e) show vertical velocity (W), c) and f) show height (z), g) and j) show kinetic dissipation rate (ε), h) and k) show supersaturation fluctuation (σ_S) and i) and l) show the evaporation rate. In each panel, the 50th, 75th, and 90th percentile values (p50, p75, p90), and Eq. 5 from Fig. 4 are indicated by solid lines in orange, magenta, red, and cyan, respectively. Values represent bin-averaged means from 3D simulation results during the final 2 hours of simulation, mapped onto the r_{m}–d_{r} phase space.

3.3.3 Entrainment and Descent regime ($S < 0$)

After the *adiabatic growth regime*, droplets enter the *entrainment and descent regime* (region C in Fig. 5e and f). In this regime, the $\dot{r_{\mathrm{m}}}$–$\dot{d_{\mathrm{r}}}$ correlation becomes negative: r_{m} decreases and d_{r} increases due to evaporation caused either by mixing with free-tropospheric air or by adiabatic heating during descent. Unlike in the previous regimes, where most droplets follow similar evolution pathways, droplet pathways diverge significantly in this regime (Fig. 4b). Notably, for rare cases of very high d_{r}, r_{m}

https://doi.org/10.5194/egusphere-2025-6099
Preprint. Discussion started: 23 December 2025
© Author(s) 2025. CC BY 4.0 License.

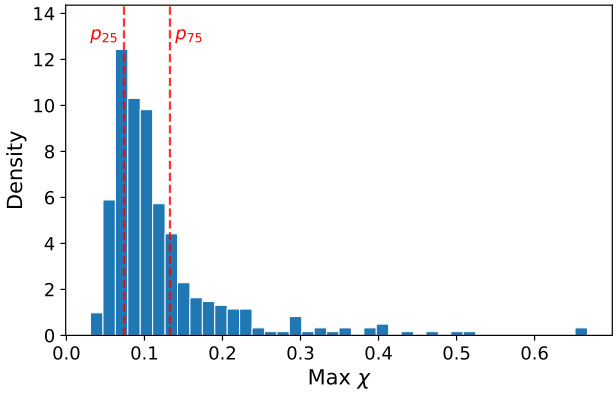

Figure 8. Density distribution of maximum χ for individual tracked particles over their lifetime in the stratocumulus-topped boundary layer. The 25th (p_{25}) and 75th (p_{75}) percentiles of the maximum χ are indicated with red dashed lines.

increases while d_r decreases (Fig. 5e and f). These represent cases of narrowing mixing (Lim and Hoffmann, 2023), wherein an extremely wide DSD narrows after mixing due to the substantial evaporation of small droplets, causing the average droplet size to increase.

While some droplets experience rapid altitude changes, following the STBL vertical circulation (indicated by the p50 line in Fig. 4), others remain near the cloud top, close to the p90 line (Fig. 7f). These latter droplets exhibit weak vertical velocity W (Fig. 7e) within negatively buoyant air (Fig. 7d) and are directly subject to entrainment and mixing. This is indicated by high ε (Fig. 7j), high σ_S (Fig. 7k), low S (Fig. 6j), and high χ (Fig. 6k). Consequently, droplets directly impacted by mixing (near the p90 line) undergo more abrupt evaporation and deactivation (Fig. 6l) compared to those following the STBL vertical circulation (near the p50 line in Fig. 4b), which experience more gradual evaporation (Fig. 7l) and lower χ (Fig. 6k).

To determine whether certain droplets escape the direct effects of entrainment and mixing (i.e., simply following the downdrafts of the STBL vertical circulation), we analyze the density distribution of maximum χ values along individual droplet trajectories (Fig. 8). The maximum χ, calculated over each droplet's lifetime from activation to deactivation, quantifies the extent of mixing influence. Trajectories with a maximum $\chi < 0.1$ indicate a relatively minor impact from entrainment. As shown in Fig. 8, a notable fraction of droplets exhibit low maximum χ values, suggesting that many are not substantially affected by active mixing events. This is consistent with Fig. 4, where some droplets descend without a significant decrease in supersaturation S or increase in χ (Fig. 6j and k) despite strong downdrafts (Fig. 7e).

The diversity of pathways in the evaporation regime contrasts with the *adiabatic growth* regime, where droplets follow nearly uniform growth paths. In the *entrainment and descent* regime, trajectories diverge: some are directly impacted by entrainment (p90 line in Fig. 7e), while others remain largely unaffected, following the strong downdraft circulation (p50 line in Fig. 7e). To better understand the evolution of these diverse pathways and how microphysical properties diverge, we show changes in mixing-related properties for individual particle trajectories in the χ–z phase space (Figs. 9 and 10). We categorized droplets based on the 25th (0.08) and 75th (0.14) percentiles of their maximum lifetime χ values (Fig. 8). Droplets directly influenced

https://doi.org/10.5194/egusphere-2025-6099
Preprint. Discussion started: 23 December 2025
© Author(s) 2025. CC BY 4.0 License.

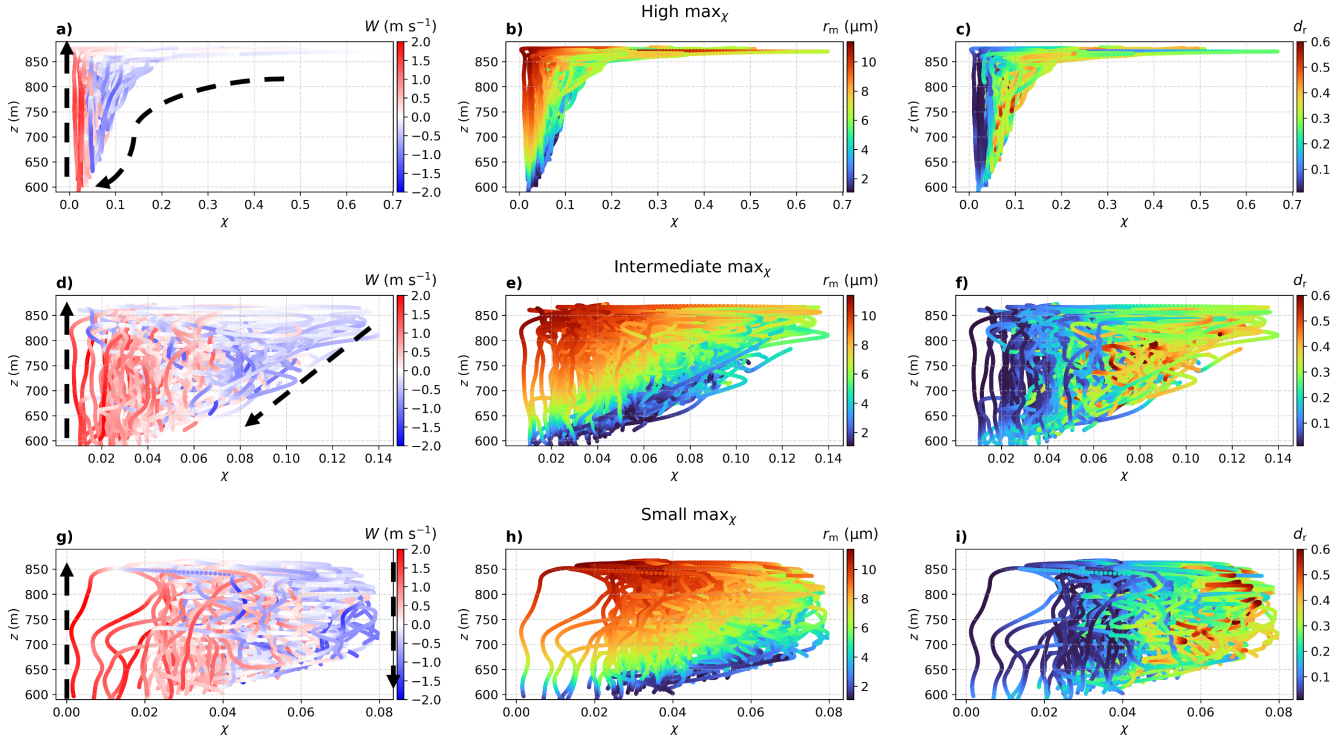

Figure 9. Particle trajectories in the $\chi - z$ phase space, where different colors of dots indicate: the W (first column), r_m (second column), d_r (third column). The first row shows trajectories with the maximum $\chi > 0.14$, the third row shows trajectories where the maximum $\chi \leq 0.08$, and the second row shows trajectories with intermediate values, where the maximum χ lies between these two conditions. In panels a), d), and g), the dashed black arrows indicate inferred droplet motion directions based on the vertical velocity W.

by mixing experience high maximum $\chi > 0.14$ (first row), while the second and third rows show droplets with intermediate ($0.08 \leq \chi \leq 0.14$) and low ($\chi < 0.08$) maximum values, respectively. In all cases, d_r remains below 0.1 during ascent and increases when $W < 0$ with higher χ (Fig. 9c, f, and i).

While most droplets descend without experiencing a substantial decrease in S, only a fraction are directly influenced by mixing, where S decreases as χ increases (Fig. 10e). For these droplets, S increases and χ decreases again after reaching its peak, indicating the restoration of S after mixing and evaporation, as well as further homogenization within the cloud. Notably, supersaturation fluctuation (σ_S) reaches a maximum at the cloud top while χ increases, further indicating entrainment and mixing. As r_m decreases and d_r increases rapidly during mixing and evaporation (Fig. 9b and c), these droplets descend and evaporate in a new state characterized by modified r_m and d_r. Conversely, droplets that do not experience high χ descend with a continuous state obtained at the end of the *adiabatic growth regime*, characterized by maximum r_m and minimum d_r (Fig. 9h and i).

Thus, for droplets not directly affected by mixing, r_m is primarily a function of altitude (Fig. 9h). At the same altitude, r_m is only slightly smaller at higher χ, regardless of whether the droplets are ascending or descending (Fig. 9g). Meanwhile, d_r is

https://doi.org/10.5194/egusphere-2025-6099
Preprint. Discussion started: 23 December 2025
© Author(s) 2025. CC BY 4.0 License.

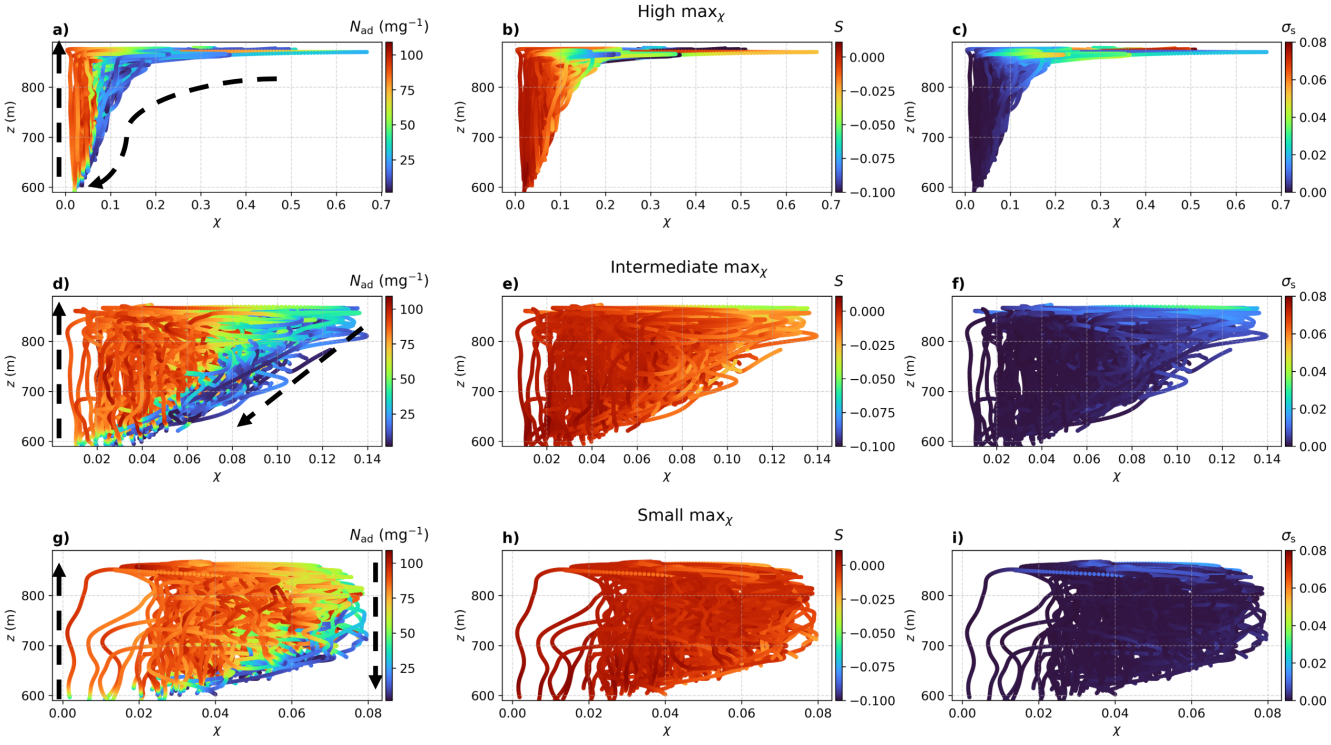

Figure 10. Particle trajectories in the $\chi - z$ phase space, where different colors of dots indicate: the N_{ad} (first column), S (second column), and σ_{S} (third column). The first row shows trajectories with the maximum $\chi > 0.14$, the third row shows trajectories where the maximum $\chi \leq 0.08$, and the second row shows trajectories with intermediate values, where the maximum χ lies between these two conditions. In panels a), d), and g), the dashed black arrows indicate inferred droplet motion directions based on the vertical velocity W.

larger during descent (Fig. 9i), indicating evaporation. Along these trajectories, S remains high, while χ and σ_S remain low, suggesting that these droplets likely ascend and descend with negligible influence from entrainment. Furthermore, while both droplet groups undergo evaporation during descent, their initial r_{m} and d_{r} differ based on whether they reached a new state after mixing. This divergence leads to distinct evolution paths in the r_{m}–d_{r} phase space.

Another difference between the ascending and descending pathways is the evolution of droplet number concentration. To separate the decrease in N_{c} caused by simple entrainment dilution from that caused by mixing-induced evaporation, we examine the dilution-corrected number concentration, defined as $N_{\mathrm{ad}} = N_{\mathrm{c}}/(1-\chi)$. Here, the subscript 'ad' denotes the adiabatic value, representing the concentration expected in an undiluted parcel. Specifically, N_{ad} is substantially lower at higher altitudes when droplets are directly affected by entrainment (Fig. 10a) compared to those not directly affected (Fig. 10g). This distinct reduction is also evident in the r_{m}–d_{r} phase space, where droplets directly impacted by entrainment exhibit a rapid decrease in N_{ad} (Fig. 10a). This decrease, representing droplet loss beyond simple dilution, is consistent with inhomogeneous mixing, wherein some droplets completely evaporate in locally subsaturated environments while others remain relatively unaltered. The localized increase in σ_S further supports the presence of LEM represented SGS supersaturation variability driving this

https://doi.org/10.5194/egusphere-2025-6099
Preprint. Discussion started: 23 December 2025
© Author(s) 2025. CC BY 4.0 License.

selective evaporation. These findings align with recent observational studies suggesting that inhomogeneous mixing signals are prevalent near the top of Sc clouds (Yeom et al., 2021).

However, we cannot ensure that $N_c/(1-\chi)$ has fully isolated the effects of evaporation from entrainment-driven dilution. While the spatial distribution of the mixing signal indicates stronger inhomogeneous characteristics near the cloud top and homogeneous-like features below, it is questionable whether changes observed below the cloud base should be interpreted as a result of active entrainment, especially since the majority of droplets descending with the STBL vertical circulation are not directly impacted by entrainment events. These uncertainties highlight a fundamental ambiguity in interpreting in situ observations of r_m and N_c as indicators of mixing type, particularly when a precise estimation of χ is unavailable.

To resolve this ambiguity, the maps of Da_{phase}, Da_{evap}, and the ratio τ_{phase}/τ_{evap} in the χ–z phase space (Fig. 11) quantify the varying inhomogeneous and homogeneous mixing signals at the same height. Here, the Damköhler number is defined generally as

$$Da = \frac{\tau_{mix}}{\tau_{micro}}, \tag{7}$$

where the mixing timescale (Baker and Latham, 1979; Baker et al., 1980) is

$$\tau_{mix} = \left(\frac{l^2}{\varepsilon}\right)^{\frac{1}{3}}. \tag{8}$$

Here, l represents the length scale of scalar inhomogeneity caused by entrainment, which breaks down to the Kolmogorov length scale through turbulent motion. Since the entrainment length scale l varies with the size of the entrained blobs, we estimate the mixing length using χ as $l = (\chi \cdot \Delta x \cdot \Delta y \cdot \Delta z)^{1/3}$. Notably, using the equivalent geometric LES grid lengthscale (≈ 7.9 m) as a proxy for l results in a larger τ_{mix} but does not alter the conclusions. The relevant microphysical timescales are the phase relaxation time

$$\tau_{phase} = \frac{1}{4\pi D_v r_m N_c} \tag{9}$$

and the evaporation timescale

$$\tau_{evap} = -\frac{r_m^2}{2GS}, \tag{10}$$

defined only in subsaturated regions with $S < 0$ (Squires, 1952; Lehmann et al., 2009; Tölle and Krueger, 2014). Here, D_v is the molecular diffusion coefficient for water vapor, and G is the condensational growth parameter. Theoretically, when $Da \gg 1$, turbulent mixing is slower than the microphysical response, favoring inhomogeneous mixing. Conversely, when $Da \ll 1$, turbulent mixing is fast enough to homogenize the subsaturated entrained air with the saturated cloud air before droplets respond, leading to homogeneous mixing.

https://doi.org/10.5194/egusphere-2025-6099
Preprint. Discussion started: 23 December 2025
© Author(s) 2025. CC BY 4.0 License.

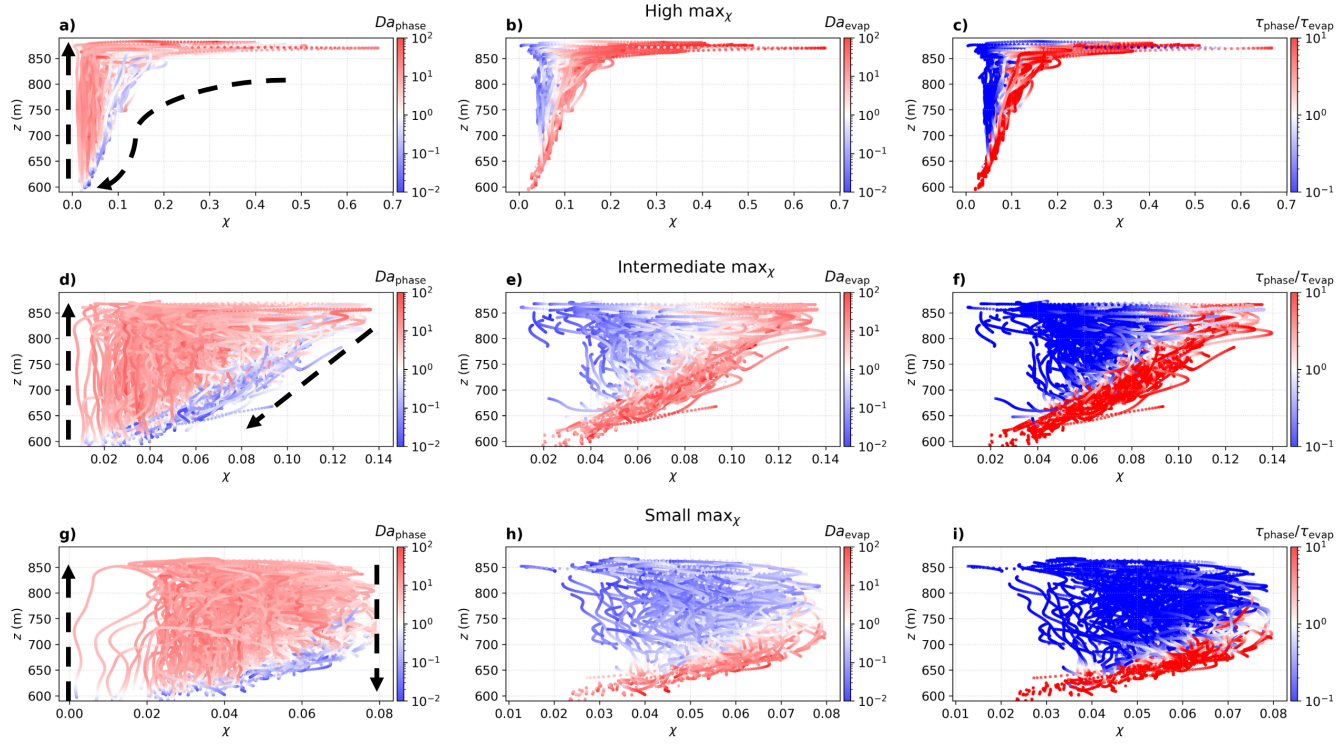

Figure 11. Particle trajectories in the χ–z phase space, where different colors of dots indicate: the Da_{phase} (first column), Da_{evap} (second column), $\tau_{\mathrm{evap}}/\tau_{\mathrm{phase}}$ (third column). The first row shows trajectories with the maximum $\chi > 0.14$, the third row shows trajectories where the maximum $\chi \leq 0.08$, and the second row shows trajectories with intermediate values, where the maximum χ lies between these two conditions. In panels a), d), and g), the dashed black arrows indicate inferred droplet motion directions based on the vertical velocity W.

While mixing scenarios have often been characterized using a single Damköhler number constructed from one microphysical response time (e.g., Baker et al., 1980; Burnet and Brenguier, 2007), recent work has highlighted the limitations of such single-parameter descriptions and the need to consider multiple thermodynamic timescales (Lehmann et al., 2009; Jeffery, 2007; Lu et al., 2018; Fries et al., 2021). Therefore, we define two Damköhler numbers:

$$Da_{\mathrm{phase}} = \frac{\tau_{\mathrm{mix}}}{\tau_{\mathrm{phase}}} \quad \text{and} \quad Da_{\mathrm{evap}} = \frac{\tau_{\mathrm{mix}}}{\tau_{\mathrm{evap}}}, \tag{11}$$

which represent the supersaturation relaxation–based and evaporation–based Damköhler numbers, respectively. Here, Da_{phase} measures how efficiently phase relaxation can restore supersaturation relative to turbulent mixing, whereas Da_{evap} measures how efficiently droplets can evaporate before the mixed air is re-saturated. In addition, we use the ratio between the two Damköhler numbers, $\tau_{\mathrm{phase}}/\tau_{\mathrm{evap}}$, which is closely related to the parameter suggested by Fries et al. (2021) and corresponds to the potential evaporation parameter of Pinsky et al. (2016).

In the high-χ regime (first row of Fig. 11), particles directly affected by entrainment frequently experience $Da_{\mathrm{phase}} > 1$ (Fig. 11a) and $Da_{\mathrm{evap}} > 1$ (Fig. 11b), together with $\tau_{\mathrm{phase}}/\tau_{\mathrm{evap}} \gtrsim 1$ (Fig. 11c). This combination is consistent with an

https://doi.org/10.5194/egusphere-2025-6099
Preprint. Discussion started: 23 December 2025
© Author(s) 2025. CC BY 4.0 License.

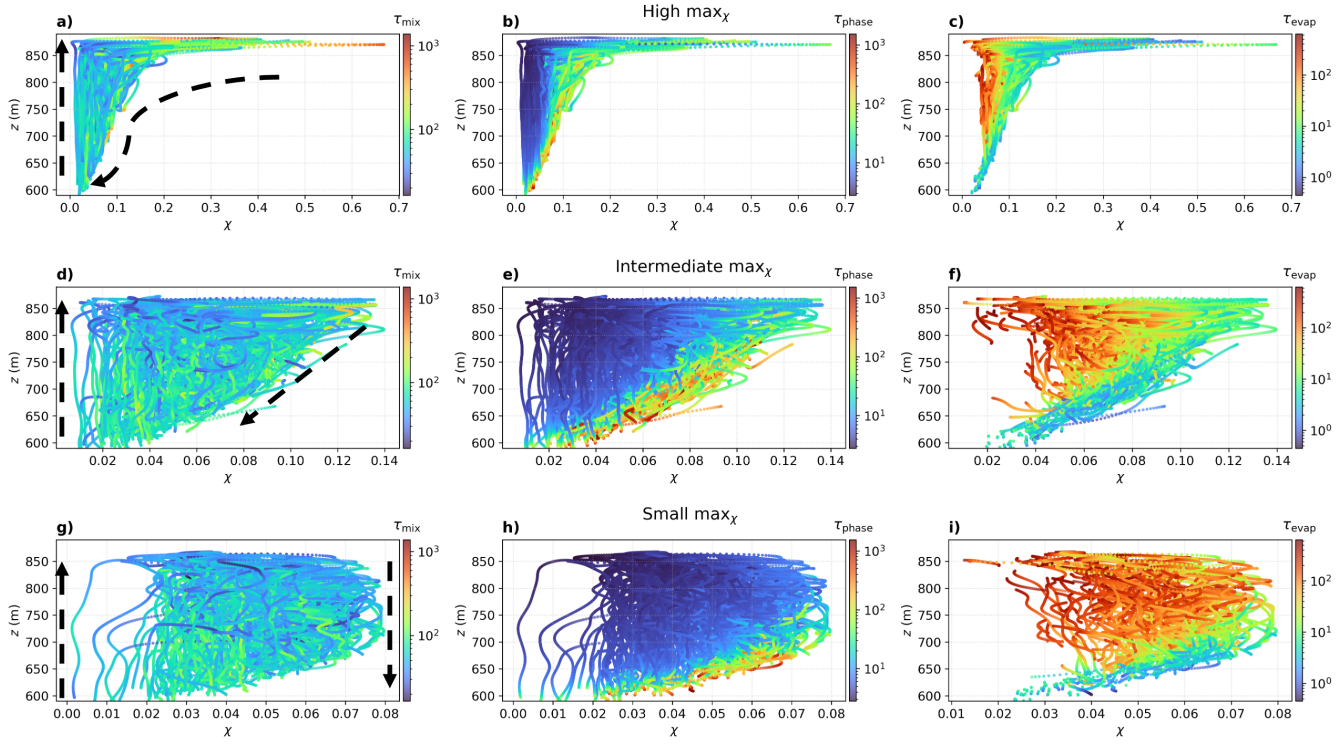

Figure 12. Particle trajectories in the χ–z phase space, where different colors of dots indicate: the mixing timescale τ_{mix} (first column), the phase-change timescale τ_{phase} (second column), and the evaporation timescale τ_{evap} (third column). The first row shows trajectories with the maximum $\chi > 0.14$, the third row shows trajectories where the maximum $\chi \leq 0.08$, and the second row shows trajectories with intermediate values, where the maximum χ lies between these two conditions. In panels a), d), and g), the dashed black arrows indicate inferred droplet motion directions based on the vertical velocity W.

inhomogeneous mixing scenario, in which a subset of droplets completely evaporates while the remaining droplets maintain a relatively large r_{m}. Interestingly, Da_{phase} tends to decrease as these droplets descend (Fig. 11a), which could be interpreted as a transition from inhomogeneous toward homogeneous-like mixing if one were to consider only τ_{phase}. However, Da_{evap} often remains larger than unity (Fig. 11b), indicating that the transition from inhomogeneous mixing near the cloud top to homogeneous mixing below is not as straightforward as suggested in recent studies (Yeom et al., 2021, 2023).

In contrast, trajectories that remain in the low-χ regime throughout their lifetime (third row of Fig. 11) tend to occupy regions with smaller Da_{evap} (Fig. 11h) but relatively large Da_{phase} (Fig. 11g), and with $\tau_{\mathrm{phase}}/\tau_{\mathrm{evap}} < 1$ (Fig. 11i). In this regime, phase relaxation is fast compared to both turbulent mixing and evaporation, whereas evaporation is comparatively slow. As a result, supersaturation is restored before droplets can fully evaporate, suppressing complete evaporation events. These conditions are consistent with a homogeneous-like response, where droplets undergo gradual changes in r_{m} and N_{c} during descent in the absence of strong small-scale supersaturation variability. Consequently, these particles show signatures of homogeneous-like mixing throughout the column when diagnosed using Da_{evap} (Fig. 11h).

https://doi.org/10.5194/egusphere-2025-6099
Preprint. Discussion started: 23 December 2025
© Author(s) 2025. CC BY 4.0 License.

The corresponding maps of the absolute timescales τ_{mix}, τ_{phase}, and τ_{evap} (Fig. 12) clarify why these diagnostics separate the regimes. The mixing timescale τ_{mix} varies relatively modestly across the χ–z phase space (Fig. 12a and g), whereas τ_{phase} and τ_{evap} exhibit much stronger spatial contrasts. Therefore, changes in Da_{phase} and Da_{evap} are driven mainly by the two microphysical timescales. The phase relaxation time τ_{phase} is strongly related to N_{c}: regions with strongly reduced N_{c} after complete evaporation events exhibit larger τ_{phase} (Fig. 12b), while most other regions show much shorter τ_{phase} (Fig. 12h). The evaporation timescale τ_{evap} behaves inversely, being large in nearly saturated regions and decreasing rapidly with increasing subsaturation (Fig. 12c and i). Taken together, using $\tau_{\mathrm{phase}}/\tau_{\mathrm{evap}}$ provides a natural separation between regimes where droplets are prone to complete evaporation and regimes where supersaturation is restored quickly enough to maintain a more homogeneous-like evolution. In contrast, relying on Da_{phase} alone would incorrectly imply inhomogeneous mixing at the cloud top in almost all cases, contradictory to our findings.

These results highlight that inhomogeneous mixing is not spatially locked to a fixed height, such as "near cloud top," but is instead determined by the Lagrangian mixing history, summarized by χ, and by the strength of entrainment and dilution. High-χ parcels maintain the signature of inhomogeneous mixing (depleted N_{c}, high Da_{evap}) well below the cloud top because they descend within air that has not been fully replenished or homogenized. Conversely, low-χ parcels can exhibit homogeneous-like characteristics even near the cloud top and retain this signature along their subsequent descent. These distinct Lagrangian histories at similar altitudes explain why snapshots of r_{m} and N_{c} at a given height can simultaneously contain the imprints of both inhomogeneous and homogeneous mixing histories.

3.3.4 Deactivation Regime ($S < 0$)

Droplets transition into the *deactivation regime* at the end of their life cycle near the cloud base (Fig. 7f). In this regime, the relationship between $\dot{r_{\mathrm{m}}}$ and $\dot{d}_{\mathrm{r}}$ is complex, as r_{m} decreases while d_{r} increases for larger r_{m}, but decreases for smaller r_{m}. The decrease in r_{m} is due to the evaporation of droplets. For larger r_{m}, d_{r} initially increases, as observed in the *entrainment and descent* regime. However, as the droplets approach complete evaporation, d_{r} decreases since only a small number of droplets remain. Therefore, this regime is opposite to the *activation regime* with substantial deactivation (Fig. 6l). Note that this regime does not overlap with the *activation regime*, because r_{m} and d_{r} are generally larger in the *deactivation regime* compared to the *activation regime*, indicating a stronger spatial variability in deactivation. Moreover, since particle trajectories are only tracked for $q_{\mathrm{c}} > 0$, an abrupt loss of liquid water near the point of complete evaporation may result in a bias toward retaining large r_{m} values as the final recorded state.

3.4 Implications for Cloud Optical Properties and Precipitation Initiation

To quantify the macroscopic impact of the divergent DSD aging pathways identified in the previous section, we examine the distribution of the effective radius (r_{e}), extinction coefficient (β_{ext}), and autoconversion rate (ATC) within the r_{m}–d_{r} phase space (Fig. 13).

https://doi.org/10.5194/egusphere-2025-6099
Preprint. Discussion started: 23 December 2025
© Author(s) 2025. CC BY 4.0 License.

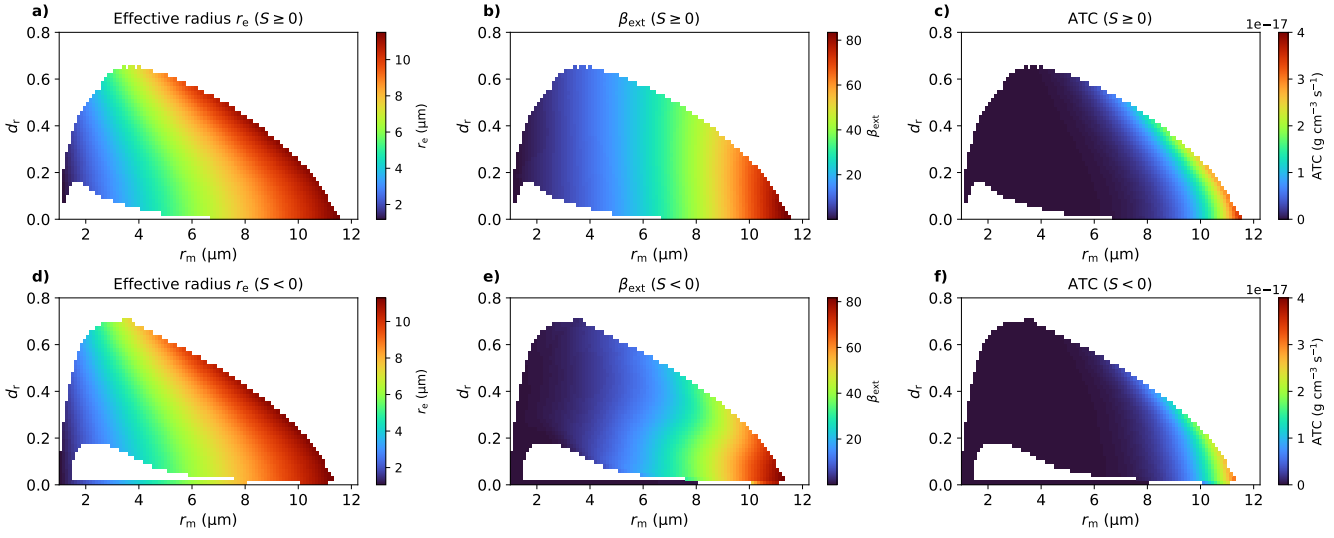

Figure 13. Contour plots in the r_m–d_r phase space for (a, d) effective radius (r_e), (b, e) extinction coefficient (β_{ext}), and (c, f) autoconversion rate (ATC). The first row shows results for $S \geq 0$ and the second row for $S < 0$.

Cloud optical properties are strongly modulated by the DSD width. Assuming a gamma distribution, the effective radius is $r_e = r_m(1 + 2d_r^2)$, and the extinction coefficient is

$$\beta_{ext} \propto q_c / r_e. \tag{12}$$

As shown in Fig. 13a and d, r_e increases with both r_m and d_r, illustrating that broader distributions result in larger effective radii for a given mean size. Note that while the functional dependence of r_e on r_m and d_r is identical in Figs. 13a and d, the regions of the phase space occupied by droplets differ between the supersaturated ($S \geq 0$) and subsaturated ($S < 0$) regimes.

In the *entrainment and descent* regime ($S < 0$), β_{ext} is primarily dominated by the reduction in liquid water content (q_c) due to evaporation (Fig. 13e). Consequently, the direct visual correlation between d_r and β_{ext} is less distinct compared to that of r_e. However, Eq. 12 implies a synergistic effect: entrainment reduces q_c through dilution and evaporation while simultaneously increasing r_e through spectral broadening. Thus, although the reduction in β_{ext} is largely driven by q_c loss, the entrainment-driven DSD broadening acts to accelerate the decrease in cloud optical depth.

Finally, we assess the susceptibility of different aging pathways to rain initiation using the autoconversion rate (ATC). We employ a modified Kessler-type parameterization that explicitly accounts for spectral shape dispersion (Liu and Daum, 2004):

$$\mathrm{ATC} \propto q_c^3 N_c^{-1} \beta_6(d_r), \tag{13}$$

where β_6 is a shape parameter that increases non-linearly with d_r. Although the simulated cloud remains largely non-precipitating ($r_m < 12$ μm), the phase space analysis reveals distinct regimes of precipitation susceptibility (Fig. 13c and f). While ATC is

https://doi.org/10.5194/egusphere-2025-6099
Preprint. Discussion started: 23 December 2025
© Author(s) 2025. CC BY 4.0 License.

generally low, it exhibits a clear sensitivity to d_r in the aging regimes. This indicates that droplets following the "broadening" pathway (high mixing fraction χ, high d_r) are preconditioned for enhanced autoconversion. Thus, the history of entrainment and mixing not only modulates local radiative cooling but may also accelerate the transition from non-precipitating to precipitating regimes by broadening the DSD prior to substantial droplet growth.

4 Summary and Conclusion

Maritime stratocumulus (Sc) clouds play an important role in Earth's radiative budget by reflecting incoming solar radiation (Wood, 2012). However, our lack of understanding of the variation of key parameters determining the cloud's optical properties, such as the droplet size distribution (DSD), makes clouds a key source of model uncertainty (Boucher et al., 2013). In this study, we investigate the evolution of droplets, focusing on how DSD shape parameters, the mean droplet radius (r_m) and droplet radius relative dispersion (d_r), evolve by tracking individual cloud droplets. For this purpose, we employ the L^3 model that couples a large-eddy simulation (LES) model with a Lagrangian cloud model (LCM), and the linear eddy model (LEM) to accurately represent entrainment and mixing, a key process in determining DSD shape (Lim and Hoffmann, 2023).

We find that the evolution of droplet size distribution (DSD) shape parameters follows characteristic trajectories in the r_m–d_r phase space, governed by the large-scale circulation of the stratocumulus-topped boundary layer (STBL). Droplets undergo distinct transitions, including activation, condensational growth, entrainment-driven evaporation, and gravitational descent, each constituting a stage of an "aging" pathway. Based on supersaturation conditions, we classify the droplet population into four microphysical regimes as follows:

1. Activation ($S \geq 0$, small r_m): droplets activate, increasing r_m and broadening d_r.
2. Adiabatic growth ($S \geq 0$, small d_r): condensational growth narrows the DSD while increasing r_m, following the analytical parcel theory ($d_r \propto r_m^{-2}$).
3. Entrainment and descent ($S < 0$): evaporation drives a decrease in r_m and an increase in d_r. Critically, droplets in this regime follow divergent pathways determined by their specific entrainment history (mixing fraction χ).
4. Deactivation ($S < 0$, near cloud base): the final evaporation stage, where large droplets persist longer than small ones, briefly widening d_r before full deactivation.

Importantly, this study helps resolve the fundamental ambiguity in interpreting mixing mechanisms in stratocumulus clouds. While vertical profiles of droplet number concentration (N_c) and mean radius (r_m) often suggest a transition from inhomogeneous mixing at the cloud top to homogeneous mixing below (Yum et al., 2015; Yeom et al., 2021), our Lagrangian analysis reveals that this vertical structure is primarily a consequence of sorting droplets by their entrainment history. By analyzing the Damköhler numbers (Da_{evap}) and mixing fraction (χ), we show that the apparent mixing regime is determined by the Lagrangian history rather than instantaneous altitude. Droplets directly impacted by entrainment (high χ) typically exhibit inhomogeneous signatures, characterized by a substantial decrease in N_c and high Da_{evap}, particularly under conditions of

https://doi.org/10.5194/egusphere-2025-6099
Preprint. Discussion started: 23 December 2025
© Author(s) 2025. CC BY 4.0 License.

strong subsaturation. However, it is worth noting that entrainment events associated with weak subsaturation can still yield homogeneous mixing signatures even at the cloud top. Conversely, the pervasive "homogeneous" mixing signal observed at lower altitudes arises largely from droplets that descend via the STBL circulation without being directly impacted by entrainment events. This demonstrates that relying solely on in situ observations of N_c can lead to misinterpretations of the underlying mixing physics.

Consequently, to provide a more accurate assessment, we suggest using the evaporation-based Damköhler number Da_{evap} or the timescale ratio $\tau_{\mathrm{phase}}/\tau_{\mathrm{evap}}$ as a diagnostic for mixing scenarios (Pinsky et al., 2016; Fries et al., 2021). This approach is supported by the fact that inhomogeneous mixing is fundamentally controlled by whether a subset of droplets can completely evaporate. In particular, $\tau_{\mathrm{phase}}/\tau_{\mathrm{evap}}$ depends only on the microphysical state variables r_m, N_c, and S and does not require explicit knowledge of τ_{mix}, making it particularly attractive.

While our regime classification spans the full vertical structure of the STBL, observational access to this regime space is inherently limited. As a result, the complete trajectory of DSD evolution remains poorly constrained in most field observations. Although some observational studies have reported phase-space patterns consistent with portions of our defined regimes (e.g., Lu et al., 2020), comprehensive vertical coverage is needed to resolve the full aging pathway. Our Lagrangian framework overcomes this methodological limitation by providing a trajectory-resolved depiction of regime transitions across the full STBL depth, offering a coherent framework for interpreting in situ observations within the broader context of cloud evolution.

Building on these regime definitions, we propose a combined analytical–empirical formulation as further detailed in Appendix A that expresses d_r as a function of r_m, capturing both the condensational narrowing during adiabatic ascent and the entrainment-driven broadening during evaporation. This unified expression provides a practical framework for incorporating DSD aging variability into microphysical parameterizations in cloud models.

Our findings underscore the significance of DSD aging in preconditioning the onset of precipitation (e.g., Seifert and Beheng, 2006). Broader DSDs, shaped by diverse droplet growth pathways and mixing histories, can enhance the potential for rain formation or reduce a cloud's ability to reflect incoming solar radiation. These results emphasize that droplet-scale evolution under varying thermodynamic and dynamic conditions governs not only the DSD shape but also key radiative and precipitation-relevant properties, highlighting the need for improved representation of DSD variability in large-scale models.

Code and data availability. Simulation output used in this study is available from the author upon request. The System for Atmospheric Modeling (SAM) code is publicly available at http://rossby.msrc.sunysb.edu/SAM.html.

Appendix A: Complete Expression of Droplet Evolution Pathway

In Sec. 3.2, we showed that the growth phase of droplet evolution follows Eq.5 from Liu et al. (2006), which describes an inverse-square dependence between d_r and r_m under condensational growth ($S \geq 0$). However, this analytical formulation does not hold for the decay phase ($S < 0$), where evaporation and mixing lead to nonlinear and path-dependent broadening. To

https://doi.org/10.5194/egusphere-2025-6099
Preprint. Discussion started: 23 December 2025
© Author(s) 2025. CC BY 4.0 License.

assess whether the analytical form can still approximate the decay branch, we refitted Eq.5 to the $S < 0$ data. The resulting fit (light-gray dashed line in Fig. A1) yields $r^2 = 0.5 - 0.8$, indicating that the inverse square dependence reproduces the overall decreasing trend of d_r with r_m, but fails to capture the curvature and saturation observed at larger droplet sizes. This mismatch reflects the inherently different physics of the evaporation regime, where droplets experience intermittent subsaturation and entrainment-driven dilution, deviating from the purely diffusional scaling assumed in Eq.5.

To better represent the curved structure in the decay regime, especially for intermediate d_r values (0.1–0.3), we generalize the formulation into a piecewise function:

$$d_\mathrm{r} = \begin{cases} d_{\mathrm{r},0} \frac{r_{\mathrm{m},0}^2}{r_\mathrm{m}^2} & \text{if } S \geq 0, \\ d_{\mathrm{r,max}} \left(1 - \frac{r_\mathrm{m}^2}{r_{\mathrm{m,max}}^2}\right) & \text{if } S < 0. \end{cases} \tag{A1}$$

The results of Eq. A1, fitted to the 50th percentile of the frequency distributions over the final 2 hours of simulation, are shown as solid lines in Fig. A1 for the N50, N100, and N200 cases. The fitted values of $d_\mathrm{r,max}$ are 0.39, 0.40, and 0.41, respectively, while $r_\mathrm{m,max}$ values are 14.9, 11.8, and 9.4 µm, with all fits yielding $r^2 > 0.98$. While $d_\mathrm{r,max}$ exhibits only modest variation across aerosol scenarios, $r_\mathrm{m,max}$ decreases noticeably with increasing N_a, consistent with liquid water being partitioned among a larger number of droplets. The relative insensitivity of $d_\mathrm{r,max}$ to N_a suggests that a fixed value in the range of 0.3–0.4, commonly observed in stratocumulus clouds (Pawlowska et al., 2006), may serve as a useful approximation.

Author contributions. JSL conceived the original conceptualization and interpretation of results and model modification. FH provided the base model, contributed to discussions, and provided the funding acquisition for the study and project administration. JSL wrote the original draft, and JSL and FH contributed to the review and editing.

Competing interests. There are no competing interests.

Acknowledgements. This work is supported by the Emmy-Noether program of the German Research Foundation (DFG) under grant HO 6588/1-1. The authors gratefully acknowledge the Gauss Centre for Supercomputing e.V. (www.gauss-centre.eu) for funding this project by providing computing time on the GCS Supercomputer SuperMUC-NG at Leibniz Supercomputing Centre (www.lrz.de).

https://doi.org/10.5194/egusphere-2025-6099
Preprint. Discussion started: 23 December 2025
© Author(s) 2025. CC BY 4.0 License.

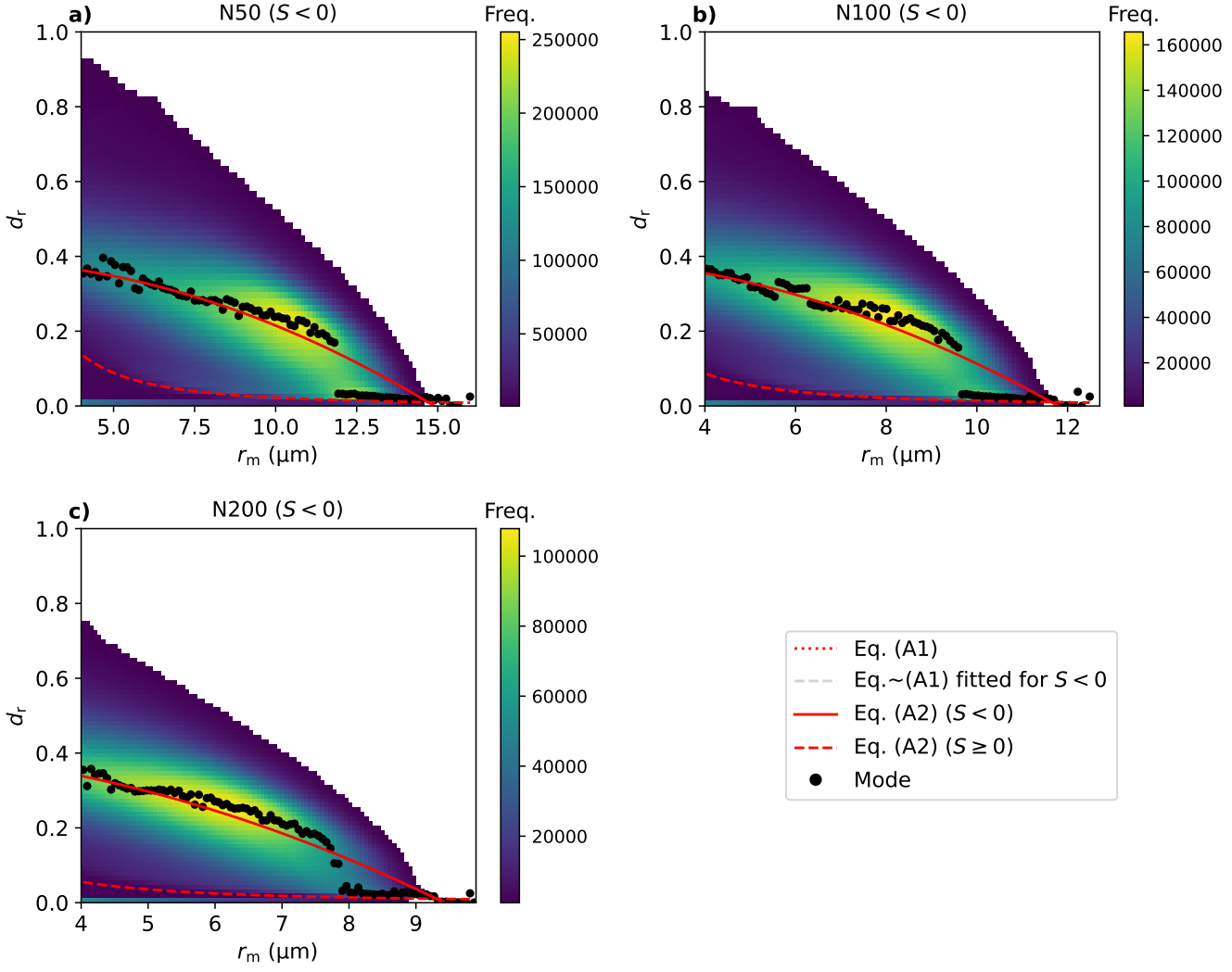

Figure A1. Frequency distribution in the r_m–d_r phase space for $S < 0$ for the a) N50, b) N100, and c) N200 cases. Black dots represent the most frequent value (mode) in each r_m bin. The light-gray dashed line shows the fit of the analytical growth-phase equation (Eq. 5) to the $S < 0$ data. The red lines represent the empirical fits for this evaporation pathway using the final quadratic formulation (the $S < 0$ part of Eq. A1 as solid and the $S \geq 0$ part of Eq. A1 as dashed). All fits are based on the median d_r value in each r_m bin.

References

Ackerman, A. S., Stevens, B., Savic-Jovcic, V., Bretherton, C. S., Chlond, A., Golaz, J.-C., Jiang, H., Khairoutdinov, M., Krueger, S. K., Lewellen, D. C., et al.: Large-eddy simulations of a drizzling, stratocumulus-topped marine boundary layer, Monthly Weather Review, 137, 1083–1110, 2009.

Baker, M. and Latham, J.: The evolution of droplet spectra and the rate of production of embryonic raindrops in small cumulus clouds, Journal of the Atmospheric Sciences, 36, 1612–1615, https://doi.org/10.1175/1520-0469(1979)036%3C1612:TEODSA%3E2.0.CO;2, 1979.

https://doi.org/10.5194/egusphere-2025-6099
Preprint. Discussion started: 23 December 2025
© Author(s) 2025. CC BY 4.0 License.

Baker, M., Corbin, R., and Latham, J.: The influence of entrainment on the evolution of cloud droplet spectra: I. A model of inhomogeneous mixing, Quarterly Journal of the Royal Meteorological Society, 106, 581–598, https://doi.org/10.1002/qj.49710644914, 1980.

Boucher, O., Randall, D., Artaxo, P., Bretherton, C., Feingold, G., Forster, P., Kerminen, V.-M., Kondo, Y., Liao, H., Lohmann, U., et al.: Clouds and aerosols, in: Climate change 2013: The physical science basis. Contribution of working group I to the fifth assessment report of the intergovernmental panel on climate change, pp. 571–657, Cambridge University Press, 2013.

Burnet, F. and Brenguier, J.-L.: Observational study of the entrainment-mixing process in warm convective clouds, Journal of the atmospheric sciences, 64, 1995–2011, 2007.

Chandrakar, K. K., Cantrell, W., and Shaw, R. A.: Influence of turbulent fluctuations on cloud droplet size dispersion and aerosol indirect effects, Journal of the atmospheric sciences, 75, 3191–3209, 2018.

Chandrakar, K. K., Morrison, H., and Witte, M.: Evolution of droplet size distributions during the transition of an ultraclean stratocumulus cloud system to open cell structure: An LES investigation using Lagrangian microphysics, Geophysical Research Letters, 49, e2022GL100 511, 2022.

Chen, T., Rossow, W. B., and Zhang, Y.: Radiative effects of cloud-type variations, Journal of climate, 13, 264–286, 2000.

Considine, G. and Curry, J. A.: A statistical model of drop-size spectra for stratocumulus clouds, Quarterly Journal of the Royal Meteorological Society, 122, 611–634, 1996.

Fries, J., Sardina, G., Svensson, G., and Mehlig, B.: Key parameters for droplet evaporation and mixing at the cloud edge, Quarterly Journal of the Royal Meteorological Society, 147, 2160–2172, 2021.

Gerber, H., Frick, G., Malinowski, S., Brenguier, J., and Burnet, F.: Holes and entrainment in stratocumulus, Journal of the atmospheric sciences, 62, 443–459, 2005.

Hoffmann, F. and Feingold, G.: Entrainment and mixing in stratocumulus: Effects of a new explicit subgrid-scale scheme for large-eddy simulations with particle-based microphysics, Journal of the Atmospheric Sciences, 76, 1955–1973, https://doi.org/10.1175/JAS-D-18-0318.1, 2019.

Hoffmann, F., Raasch, S., and Noh, Y.: Entrainment of aerosols and their activation in a shallow cumulus cloud studied with a coupled LCM–LES approach, Atmospheric Research, 156, 43–57, 2015.

Hoffmann, F., Yamaguchi, T., and Feingold, G.: Inhomogeneous mixing in Lagrangian cloud models: Effects on the production of precipitation embryos, Journal of the Atmospheric Sciences, 76, 113–133, https://doi.org/10.1175/JAS-D-18-0087.1, 2019.

Jeffery, C. A.: Inhomogeneous cloud evaporation, invariance, and Damköhler number, Journal of Geophysical Research: Atmospheres, 112, 2007.

Kerstein, A. R.: A linear-eddy model of turbulent scalar transport and mixing, Combustion Science and Technology, 60, 391–421, https://doi.org/10.1080/00102208808923995, 1988.

Khairoutdinov, M. F. and Randall, D. A.: Cloud resolving modeling of the ARM summer 1997 IOP: Model formulation, results, uncertainties, and sensitivities, J. Atmos. Sci., 60, 607–625, https://doi.org/10.1175/1520-0469(2003)060%3C0607:CRMOTA%3E2.0.CO;2, 2003.

Korolev, A. and Mazin, I.: Zones of increased and decreased droplet concentration in stratiform clouds, Journal of Applied Meteorology (1988-2005), pp. 760–773, 1993.

Krueger, S. K.: Linear eddy modeling of entrainment and mixing in stratus clouds, Journal of the atmospheric sciences, 50, 3078–3090, https://doi.org/10.1175/1520-0469(1993)050%3C3078:LEMOEA%3E2.0.CO;2, 1993.

Krueger, S. K., Su, C.-W., and McMurtry, P. A.: Modeling entrainment and finescale mixing in cumulus clouds, Journal of the atmospheric sciences, 54, 2697–2712, https://doi.org/10.1175/1520-0469(1997)054<2697:MEAFMI>2.0.CO;2, 1997.

https://doi.org/10.5194/egusphere-2025-6099
Preprint. Discussion started: 23 December 2025
© Author(s) 2025. CC BY 4.0 License.

Lehmann, K., Siebert, H., and Shaw, R. A.: Homogeneous and inhomogeneous mixing in cumulus clouds: Dependence on local turbulence structure, Journal of the Atmospheric Sciences, 66, 3641–3659, https://doi.org/10.1175/2009JAS3012.1, 2009.

Lim, J. S.: Entrainment, mixing, and the evolution of the cloud droplet size distribution, Ph.D. thesis, Ludwig-Maximilians-Universität München, Munich, Germany, 2024.

Lim, J.-S. and Hoffmann, F.: Between Broadening and Narrowing: How Mixing Affects the Width of the Droplet Size Distribution, Journal of Geophysical Research: Atmospheres, 128, e2022JD037 900, 2023.

Lim, J.-S. and Hoffmann, F.: Life cycle evolution of mixing in shallow cumulus clouds, Journal of Geophysical Research: Atmospheres, 129, e2023JD040 393, 2024.

Liu, Y. and Daum, P. H.: Parameterization of the autoconversion process. Part I: Analytical formulation of the Kessler-type parameterizations, Journal of the atmospheric sciences, 61, 1539–1548, 2004.

Liu, Y., Daum, P. H., and Yum, S. S.: Analytical expression for the relative dispersion of the cloud droplet size distribution, Geophysical research letters, 33, 2006.

Liu, Y., Daum, P. H., Guo, H., and Peng, Y.: Dispersion bias, dispersion effect, and the aerosol–cloud conundrum, Environmental Research Letters, 3, 045 021, 2008.

Lu, C., Liu, Y., Zhu, B., Yum, S. S., Krueger, S. K., Qiu, Y., Niu, S., and Luo, S.: On which microphysical time scales to use in studies of entrainment-mixing mechanisms in clouds, Journal of Geophysical Research: Atmospheres, 123, 3740–3756, 2018.

Lu, C., Liu, Y., Yum, S. S., Chen, J., Zhu, L., Gao, S., Yin, Y., Jia, X., and Wang, Y.: Reconciling contrasting relationships between relative dispersion and volume-mean radius of cloud droplet size distributions, Journal of Geophysical Research: Atmospheres, 125, e2019JD031 868, 2020.

Luo, S., Lu, C., Liu, Y., Li, Y., Gao, W., Qiu, Y., Xu, X., Li, J., Zhu, L., Wang, Y., et al.: Relationships between Cloud Droplet Spectral Relative Dispersion and Entrainment Rate and Their Impacting Factors, Advances in Atmospheric Sciences, pp. 1–20, https://doi.org/10.1007/s00376-022-1419-5, 2022.

Mellado, J. P.: Cloud-top entrainment in stratocumulus clouds, Annual Review of Fluid Mechanics, 49, 145–169, 2017.

Pawlowska, H., Grabowski, W. W., and Brenguier, J.-L.: Observations of the width of cloud droplet spectra in stratocumulus, Geophysical research letters, 33, 2006.

Pinsky, M., Khain, A., Korolev, A., and Magaritz-Ronen, L.: Theoretical investigation of mixing in warm clouds–Part 2: Homogeneous mixing, Atmospheric Chemistry and Physics, 16, 9255–9272, https://doi.org/10.5194/acp-16-9255-2016, 2016.

Seifert, A. and Beheng, K. D.: A two-moment cloud microphysics parameterization for mixed-phase clouds. Part 1: Model description, Meteorology and atmospheric physics, 92, 45–66, 2006.

Shima, S.-i., Kusano, K., Kawano, A., Sugiyama, T., and Kawahara, S.: The super-droplet method for the numerical simulation of clouds and precipitation: A particle-based and probabilistic microphysics model coupled with a non-hydrostatic model, Quarterly Journal of the Royal Meteorological Society: A journal of the atmospheric sciences, applied meteorology and physical oceanography, 135, 1307–1320, https://doi.org/10.1002/qj.441, 2009.

Siebesma, A. P., Jakob, C., Lenderink, G., Neggers, R., Teixeira, J., Van Meijgaard, E., Calvo, J., Chlond, A., Grenier, H., Jones, C., et al.: Cloud representation in general-circulation models over the northern Pacific Ocean: A EUROCS intercomparison study, Quarterly Journal of the Royal Meteorological Society: A journal of the atmospheric sciences, applied meteorology and physical oceanography, 130, 3245–3267, 2004.

https://doi.org/10.5194/egusphere-2025-6099
Preprint. Discussion started: 23 December 2025
© Author(s) 2025. CC BY 4.0 License.

Squires, P.: The growth of cloud drops by condensation. I. General characteristics, Australian Journal of Chemistry, 5, 59–86, https://doi.org/10.1071/CH9520059, 1952.

Stevens, B.: Entrainment in stratocumulus-topped mixed layers, Quarterly Journal of the Royal Meteorological Society: A journal of the atmospheric sciences, applied meteorology and physical oceanography, 128, 2663–2690, 2002.

Stevens, B., Lenschow, D. H., Vali, G., Gerber, H., Bandy, A., Blomquist, B., Brenguier, J.-L., Bretherton, C., Burnet, F., Campos, T., et al.: Dynamics and chemistry of marine stratocumulus—DYCOMS-II, Bulletin of the American Meteorological Society, 84, 579–594, 2003.

Tölle, M. H. and Krueger, S. K.: Effects of entrainment and mixing on droplet size distributions in warm cumulus clouds, Journal of Advances in Modeling Earth Systems, 6, 281–299, https://doi.org/10.1002/2012MS000209, 2014.

Virtanen, P., Gommers, R., Oliphant, T. E., Haberland, M., Reddy, T., Cournapeau, D., Burovski, E., Peterson, P., Weckesser, W., Bright, J., van der Walt, S. J., Brett, M., Wilson, J., Millman, K. J., Mayorov, N., Nelson, A. R. J., Jones, E., Kern, R., Larson, E., Carey, C. J., Polat, İ., Feng, Y., Moore, E. W., VanderPlas, J., Laxalde, D., Perktold, J., Cimrman, R., Henriksen, I., Quintero, E. A., Harris, C. R., Archibald, A. M., Ribeiro, A. H., Pedregosa, F., van Mulbregt, P., and SciPy 1.0 Contributors: SciPy 1.0: Fundamental Algorithms for Scientific Computing in Python, Nature Methods, 17, 261–272, https://doi.org/10.1038/s41592-019-0686-2, 2020.

Wang, Y., Zhao, C., McFarquhar, G. M., Wu, W., Reeves, M., and Li, J.: Dispersion of droplet size distributions in supercooled non-precipitating stratocumulus from aircraft observations obtained during the southern ocean cloud radiation aerosol transport experimental study, Journal of Geophysical Research: Atmospheres, 126, e2020JD033 720, 2021.

Wood, R.: Stratocumulus clouds, Monthly Weather Review, 140, 2373–2423, 2012.

Yau, M. K. and Rogers, R. R.: A short course in cloud physics, Elsevier, 1996.

Yeom, J. M., Yum, S. S., Shaw, R. A., La, I., Wang, J., Lu, C., Liu, Y., Mei, F., Schmid, B., and Matthews, A.: Vertical variations of cloud microphysical relationships in marine stratocumulus clouds observed during the ACE-ENA campaign, Journal of Geophysical Research: Atmospheres, 126, e2021JD034 700, 2021.

Yeom, J. M., Helman, I., Prabhakaran, P., Anderson, J. C., Yang, F., Shaw, R. A., and Cantrell, W.: Cloud microphysical response to entrainment and mixing is locally inhomogeneous and globally homogeneous: Evidence from the lab, Proceedings of the National Academy of Sciences, 120, e2307354 120, 2023.

Yum, S. S., Wang, J., Liu, Y., Senum, G., Springston, S., McGraw, R., and Yeom, J. M.: Cloud microphysical relationships and their implication on entrainment and mixing mechanism for the stratocumulus clouds measured during the VOCALS project, Journal of Geophysical Research: Atmospheres, 120, 5047–5069, 2015.